Simultaneous Determination of Relative Permeability and Capillary Pressure from an Unsteady-State Core Flooding Experiment?

Steffen Berg[a,*], Harm Dijk[b], Evren Unsal[c], Ronny Hofmann[d], Bochao Zhao[e], Vishal Ahuja[f]

[*] Corresponding author: steffen.berg@shell.com

[a] Shell Global Solutions International B.V., Grasweg 31, 1031HW Amsterdam, NL, ORCID: 0000-0003-2441-7719

[b] Shell Global Solutions International B.V., Lange Kleiweg 40, 2288 GK Rijswijk, Netherlands, ORCID: 0000-0001-6922-2689

[c] Shell Global Solutions International B.V., Grasweg 31, 1031HW Amsterdam, NL, ORCID: 000-0001-7275-7684

[d] Shell International Exploration & Production Inc., 3333 HW6 South, Shell Technology Center Houston, Houston, TX, 77024, United States, ORCID: 0000-0002-4682-270X

[e] Shell International Exploration & Production Inc., 3333 HW6 South, Shell Technology Center Houston, Houston, TX, 77024, United States, ORCID: 0000-0002-8542-056X

[f] Shell India Markets Private Limited, Shell Technology Centre Bangalore, Plot No 7, Bangalore Hardware Park, Devanahalli Industrial Park, Mahadeva Kodigehalli, Bengaluru 562149, Karnataka, India, ORCID: 0000-0003-4636-825X

ARTICLE INFO

Keywords:

Inverse modelling

Relative permeability

Capillary pressure

Flow simulation

Authorship contribution statement

Author 1: conceptualized the work, contributed to code development, performed the simulations, wrote the manuscript.

Author 2: conceptualized the work, wrote key parts of the code and validated the code, edited the manuscript

Author 3: conceptualized the work, wrote and edited the manuscript

Author 4: provided the application case, validated the code, edited the manuscript

Author 5: provided the application case, validated the code, edited the manuscript

Author 6: tested the code, supported OpenSource release of code, edited the manuscript

ABSTRACT

For modelling studies of underground storage of carbon dioxide and hydrogen, it is important to have a consistent set of relative permeability and capillary pressure-saturation functions. For consistency reasons, it is an advantage to determine both in one single experiment using the same rock and fluid sample, however, experimental measurements typically have challenges. While unsteady-state type of flow experiments is in principle suited for deriving relative permeability and capillary pressure functions, we provide a methodology to optimize the experimental settings such that the simultaneous determination of these functions can succeed within an acceptable uncertainty range, which involve multi-rate flow experiments and in-situ saturation monitoring. We provide details of the inverse modelling methodology which is a self-contained Python code that includes both the 1D flow model and the optimization method for the assisted history match. This methodology can be used for interpreting experiments, but also to optimize the design of the experiment and to reach a desired/acceptable uncertainty range. The purpose of this work is to provide the concrete assessment of unsteady-state type of experiments with the purpose of simultaneously obtaining relative permeability and capillary pressure-saturation functions by means of a ground-truth example, to detail the methodology used and make the Python code with a self-contained 1D flow solver accelerated by the `numba` just-in-time compiler publicly available. The results underline that the simultaneous determination of relative permeability and capillary pressure-saturation functions are possible only in specially designed multi-rate experiments where several saturation profiles before breakthrough are captured and the capillary end-effect is fully resolved. These conditions are not necessarily met for the more general type of unsteady-state experiments typically used in the more general Special Core Analysis (SCAL).

1. Introduction

The underground storage of carbon dioxide (CO_2) and hydrogen (H_2) are considered as potential applications for accelerating the energy transition strategies (IPPC 2005, Bui et al. 2018, Flesch et al. 2018, Gabrielli et al. 2020, Tarkowski et al., 2021). While the underground storage of CO_2 is mainly for (utilization and) sequestration purpose (IPPC 2005, Szukczewski et al. 2012, Krevor et al. 2015, Bui et al. 2018) the underground storage of H_2 is mainly intended as seasonal storage (Carden & Paterson 1979, Lord et al. 2014, Gabrielli et al. 2020). For the assessment of feasibility and the development of respective storage sites which are underground formations of rock, for instance, in depleted oil and gas fields, or in saline aquifers, numerical models are employed (Cavanagh & Hazeldine 2014, Shao et al. 2022, Saló-Salgado et al. 2023). The need for such models ranges from estimating the storage capacity and the plume migration (Shao et al 2022) to assessing risks such as potential leakage or the stability of the displacement (Berg & Ott 2012). In these models, the underground formations are discretized in grid blocks populated with the respective properties that are relevant for flow, such as porosity, permeability, but also relative permeability and capillary pressure-saturation functions (Benham et al. 2021A, Benham et al. 2021B, Shao et al. 2022, Saló-Salgado et al. 2023).

While there is already a wealth of relative permeability and capillary pressure measurements reported in the literature, these are mainly in the context of hydrocarbon recovery and much less for (supercritical) CO_2 (Bennion & Bachu 2005, Bennion & Bachu 2007, Berg et al. 2013, Burnside & Naylor 2014, Zhou et al. 2019, and references therein) and only very few for H_2 (Yekta et al. 2018, Rezaei et al. 2022). The lack of experimental data for H_2-brine relative permeability has therefore been already the motivation for utilizing pore scale modelling (Hashemi et al. 2021a). Both relative permeability and capillary pressure relations are highly dependent on the wetting properties of the rock and CO2 that it in the pore space of the rock (Anderson 1987a, Anderson 1987b, Abdallah et al. 2007), directly influencing parameters such as trapping of CO_2 (Krevor et al. 2015, Al-Menhali & Krevor 2016) and field significant field scale impact for H_2 storage (Pan et al. 2023). Previous research suggests that supercritical CO_2 may not behave like a fully non-wetting fluid (towards hydrophilic rock) like n-decane but appears to have different wetting behavior (Berg et al. 2013, Saraji et al. 2013) or mineral-specific sensitivity to CO_2 in terms of wetting behavior (Krevor et al. 2012, Farokhpoor et al. 2013). Furthermore, recent experimental observations suggest that H_2 may have different wetting behavior compared to N_2 (Iglauer et al. 2020, Pan et al. 2021, Hashemi et al. 2021, Hashemi et al. 2022, Lysyy et al. 2022) or strong hysteresis (Lysyy et al. 2022a).

It is recommended that the respective relative permeability needs to be experimentally measured with the actual fluids such as CO_2 and H_2 at relevant pressure and temperature conditions (because relevant properties may critically depend on the conditions). The preferred method to experimentally measure relative permeability is the steady-state method (Maini et al. 1990, Sorop et al. 2015) which provides a wider accessible saturation range (Berg et al. 2020) to being more robust against displacement instabilities (Berg et al. 2013 and Berg et al. 2012) and an easier interpretability compared with other methods such as the unsteady-state method. However, the steady-state method requires injection of thousands of pore volumes of fluid at varying fractional flow rates. For the case of CO_2 and H_2 that may be pose significant technical challenges on the side of the experimental setup and handling of fluids, but also may create issues around reactions between (dissolved) CO_2 or H_2 and minerals that may show in the case of CO_2 rock dissolution (Singh et al. 2018) or in the case of H_2 mineral reactions (Flesch et al. 2018).

In addition, the capillary pressure-saturation function also needs to be measured experimentally, for the same fluid pairs i.e. CO_2 or H_2 and brine, and for the process of interest (drainage or imbibition), in order to be consistent also with the relative permeability-saturation function. However, it is quite challenging to measure capillary pressure-saturation functions for live fluids (fluids saturated with gasses) and gasses as most of the industry-standard equipment such as the centrifuge method are by default not equipped for that.

Several authors have indeed demonstrated that it is possible to conduct steady-state experiments with e.g. supercritical CO_2 and were able to simultaneously determine relative permeability and capillary pressure (Pini & Benson 2013). Borazjani et al. 2021 and Hemmati et al. 2022 used a steady-state approach and in addition also the transient unsteady-state periods when changing fractional flow to determine both relative permeability and capillary pressure. Even though it has been recently demonstrated that it is indeed possible to perform steady-state relative experiments also with H_2 (Lysyy et al. 2022a), one attractive option is to consider instead the unsteady-state method which is better suited for handling the fluids of interest such as CO_2 or H_2 and operates generally at much less injection volumes than the steady-state method which is more favorable from a laboratory perspective in particular for H_2 from a safety perspective (Rezaei et al. 2022). Under specific operating conditions the unsteady-state method also allows to simultaneously determine relative permeability and capillary pressure-saturation functions as demonstrated e.g. by Berg et al. 2013. However, being actually able to determine relative permeability and capillary pressure within acceptable uncertainty ranges is not always possible and it largely depends on how exactly the experiment is conducted and which quantities are measured (e.g., in-situ measurement of saturation distribution or

profiles) and used to constrain the interpretation model. However, in many studies published in the literature that is often not fully appreciated and instead, the need for the simultaneous determination of relative permeability and capillary pressure-saturation for a live fluid such as CO_2 or H_2 is so large that also new non-standard methods (Yekta et al. 2018, Ramakrishnan & Cappiello 1991, Higgs et al. 2022) or capillary pressure derived relative permeability relationships are used (Moodie et al. 2019) which are sometimes difficult to validate. Experimental protocols and interpretation methodology can impact the resulting relative permeability much more than e.g. uncertainties around wettability which have been demonstrated cause significant differences at reservoir scale (Pan et al. 2023). Therefore, it is important to consider the impact of the measurement and interpretation protocols themselves, in particular the systematic uncertainties.

Traditional interpretation methods for unsteady-state type of experiments are often based on analytical models. Although they have significantly improved (Almutairi et al. 2022, Ge et al. 2022) to also capture the impact of the capillary end-effect, they still make often significant simplifications, and in most cases do not integrate all the experimentally measured quantities such as saturation profiles which can be obtained by in-situ X-ray saturation monitoring (Masalmeh et al. 2014) or CT scanning (Berg et al. 2013). Numerical interpretation by inverse modelling is much more reliable and provides also diagnostic capability to check for consistency and, therefore, has become the de-facto industry standard in the special core analysis (SCAL) domain (Masalmeh et al. 2014, Sorop et al. 2015). The interpretation of unsteady-state experiments by inverse modelling (Maas & Schulte 1997, Masalmeh et al. 2014, Sorop 2015) can be performed in a manual fashion i.e., by tuning relative permeability and capillary pressure-saturation functional manually to match the experimentally measured quantities such as production curve and pressure drop (Masalmeh et al. 2014, Sorop et al. 2015). However, performing the inverse modelling in an assisted fashion using optimization methods (Maas et al. 2011, Lenormand et al. 2016, Maas et al. 2019, Taheriotaghsara 2020a, Taheriotaghsara et al. 2020b, Manasipov & Jenei 2020, Berg et al. 2020, Amrollahinasab et al. 2022, Rezaei et al. 2022) or Markov-chain Monte Carlo approaches (Valdez et al. 2020, Valdez et al. 2021, Berg et al. 2021, Ranaee et al. 2022, Amrollahinasab et al. 2022 & 2023) provides also the uncertainty ranges of the relative permeability and capillary pressure-saturation functions. This additional insight allows for better clarification of the question under which conditions and protocols we can expect to determine relative permeability and capillary pressure-saturation functions from an unsteady-state experiment, and when that attempt is associated with unacceptably large uncertainty ranges.

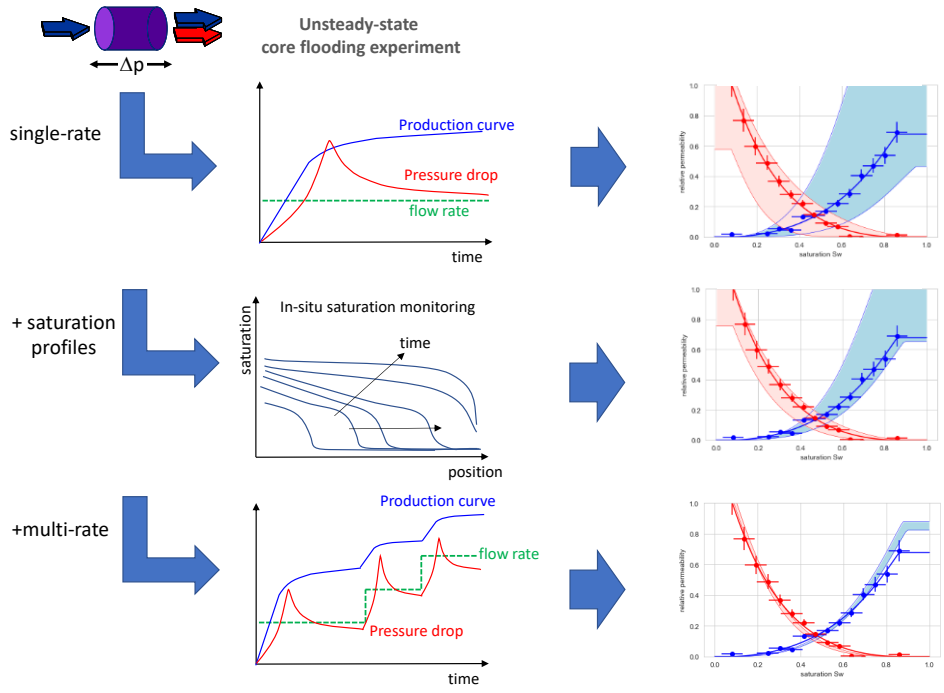

Figure 1 Unsteady-state core flooding experiment conducted at a single flow rate, adding saturation profiles from in-situ saturation monitoring and performing the experiment at multiple flow rates – impact on relative permeability uncertainty ranges.

In order to answer this question, we adopted an inverse modelling approach that was developed previously (Berg et al. 2020, Berg et al. 2021). The model was a self-contained set of Python codes that included a 1D Python-based Darcy scale flow simulator with capillarity that was accelerated with the `numba` just-in-time compiler. The simulator was applied to a synthetically generated data set that served as a ground-truth. Systematically, additional data was added, i.e., saturation profiles or multiple flow rates as additional constraint and observed its impact on the resulting uncertainty ranges for relative permeability. The workflow is sketched in Figure 1.

By following this methodology, we have concluded that relative permeability and capillary pressure relations could simultaneously be obtained from unsteady-state experiments *only* if the experiment was performed at multiple flow rates, and in-situ measured saturation profiles were used in the objective function that capture several steps of flow front before breakthrough and also captures the capillary dispersion zone within the domain size i.e. sample length.

The purpose of this work is to design a visual assessment method that can be used to determine the conditions where the capillary pressure-saturation function is an output of an unsteady-state experiment, or rather a required input for the correct interpretation of relative permeability. The purpose was also to detail the methodology and made the respective numerical codes publicly available.

2. Methodology

The inverse modelling workflow means, in practice, that the numerical solution of a flow model was fitted to experimentally measured data from core flooding experiments. The heart of the methodology used here was a ground-truth validation of the workflow sketched in Figure 2 which involved of 4 elementary steps:

1. Flow model
2. Cost function
3. Optimization
4. Uncertainty ranges

The optimization method, either the gradient-based Levenberg-Marquardt method (Levenberg 1944, Marquardt 1963) or a Markov-chain Monte Carlo (MCMC) approach, achieved a match between a numerical solution of the partial differential equations of the flow model and the reference data set, e.g., experimentally measured data (Berg et al. 2020, Berg et al. 2021). In the context of this work, for the purpose of performing a ground-truth validation, a synthetic data set was used, consisting of

- Production curve (produced non-wetting phase as function of injected pore volumes of wetting phase)
- Pressure drop Δp
- Saturation profiles $S_w(x)$ as function of position x

This ground-truth data set (with a small degree of noise) is then used as fictitious experimental data set which was subjected to the inverse modelling workflow as sketched in Figure 2.

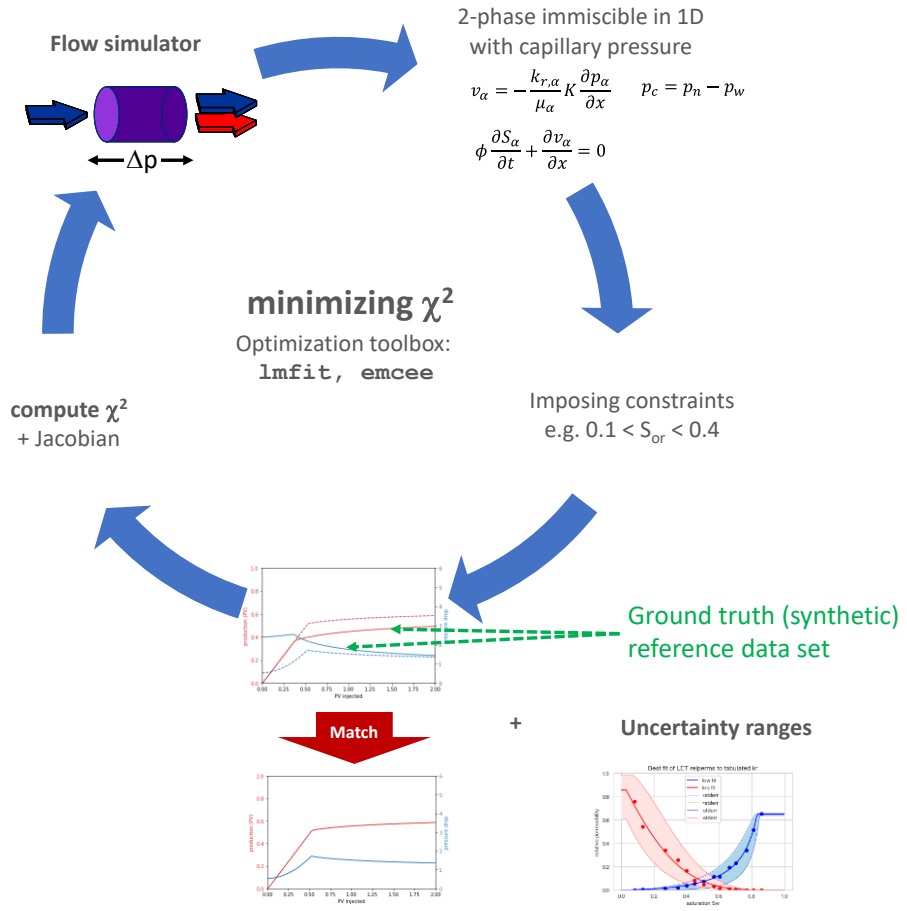

Figure 2 In the inverse modelling workflow effectively a numerical model (the numerical solution of the 2-phase Darcy and continuity partial differential equations) is fitted to data by minimizing the cost function χ^2 is using either classical gradient-based (Levenberg-Marquardt) or Markov-chain Monte Carlo (MCMC) methods. The uncertainties are then obtained either from the covariance matrix for the gradient method and from the posterior distribution (MCMC).

Hence, the inverse modelling workflow contained a numerical flow solver for the 2-phase Darcy flow model and an optimization scheme which called the flow solver and achieved the match by minimization of the cost function (or maximization of the likelihood).

2.1. Two-phase Darcy Flow Model

The two-phase flow model used the extended two-phase Darcy equations (Dake 1978, Leveque 1990)

$$v_\alpha = -\frac{k_{r,\alpha}}{\mu_\alpha} K \frac{\partial p_\alpha}{\partial x} \quad (1)$$

to relate the Darcy velocity v (which is the flow rate q divided by the cross-sectional area A i.e., $q = v \cdot A$) to the pressure gradient $\partial p/\partial x$ for a 1-dimensional flow in x-direction. The index α represents the wetting and non-wetting phases, respectively. Here, for simplicity, we labelled the wetting phase as water phase and the non-wetting phase as oil phase (which can equally well represent a gas such as H_2 or CO_2). μ_α represented the viscosity of phase α and $k_{r,\alpha}(S_w)$ was the associated relative permeability. Note that, this was for simplicity formulated in absence of gravity, which would then need to be added to the pressure gradient.

The continuity equation represented the conservation of mass where saturation changed over time t were related to the divergence of the flow

$$\phi \frac{\partial S_\alpha}{\partial t} + \frac{\partial v_\alpha}{\partial x} = 0 \quad (2)$$

Furthermore, we assumed incompressible flow where the total flux $v_T = v_w + v_o$ was constant. Also, the sum of water and oil saturation $S_w + S_o = 1$. The system of equations was closed by relating the pressure difference of water and oil to the capillary pressure

$$p_w - p_o = p_c(S_w) \quad (3)$$

Defining the mobility $\lambda_\alpha = k_{r,\alpha}/\mu_\alpha$ for phase α and the fractional flow

$$f_w = \frac{\lambda_w}{\lambda_w + \lambda_n} \quad (4)$$

Combination of eq.(1)-(4) leads to

$$\phi \frac{\partial S_w}{\partial t} + \frac{\partial}{\partial x}[f_w v_T] + \frac{\partial}{\partial x}\left[f_w \lambda_n \frac{\partial p_c}{\partial x}\right] = 0 \quad (5)$$

which describes the evolution of saturation $S_w(x,t)$ in space and time.

In this work eq. (5) is solved numerically. From the numerical solution the production curve

$$\mathrm{Q}(t) = \int_0^L S_w(x,t)dx \quad (6)$$

can be computed by integrating the saturation profile over the computational domain in x.

2.2. Parameterization of Relative Permeability and Capillary Pressure

For the parameterization of relative permeability, we used the Corey (Corey 1954) and LET models (Lomeland et al. 2005). First, we defined the reduced or mobile saturation

$$S_{red} = \frac{S_w - S_{w,c}}{1 - S_{w,c} - S_{n,r}} \quad (7)$$

$S_{w,c}$ is the irreducible or connate water saturation. $S_{n,r} = S_{o,r}$ is the irreducible or residual oil saturation.

The Corey model (Corey 1954) is essentially a power law of reduced saturation for wetting w and non-wetting n phase relative permeability

$$k_{r,w} = k_{r,w}^0 (S_{red})^{n_w}$$
$$k_{r,n} = k_{r,n}^0 (1 - S_{red})^{n_n} \quad (8)$$

where $k_{r,w}^0 = k_{r,w}(S_{n,r})$ and $k_{r,n}^0 = k_{r,n}(S_{w,c})$ are the endpoint relative permeability for water and oil, respectively. n_w and n_n are the so-called Corey parameters and define the curvedness of the relative permeability-saturation relationship.

While the Corey model describes the experimental relative permeability data, in many cases, sufficiently well, it was found to be too constraining at times (Berg et al. 2020, Berg et al. 2021). The LET model (Lomeland et al. 2005) provided more degrees of freedom and was considered generally more suitable for inverse modelling (Lenormand et al. 2016)

$$k_{r,w} = k_{r,w}^0 \frac{S_{red}^{L_w^n}}{S_{red}^{L_w^n} + E_w^n (1 - S_{red})^{T_w^n}}$$
$$k_{r,n} = k_{r,n}^0 \frac{(1 - S_{red})^{L_n^w}}{(1 - S_{red})^{L_n^w} + E_n^w S_{red}^{T_n^w}} \quad (9)$$

with the phenomenological parameters L_w^n, L_n^w, E_w^n, E_n^w, T_w^n, and T_n^w that define the shape of $k_r(S_w)$.

For the capillary pressure-saturation function $p_c(S_w)$ we use the model from Skjaeveland et al. 1998

$$p_c = \frac{c_w}{\left(\frac{S_w - S_{w,c}}{1 - S_{w,c}}\right)^{a_w}} + \frac{c_n}{\left(\frac{S_n - S_{n,r}}{1 - S_{n,r}}\right)^{a_w}} \quad (10)$$

where $S_n = 1 - S_w$ and c_w, c_n, a_w and a_n are adjustable parameters

2.3. Objective function

Fitting a model to experimental data is achieved by minimizing an objective function which is based on the concept of

$$\chi^2 = \sum_i \frac{(y_i - f(x_i))^2}{\epsilon_i^2} \quad (11)$$

where y_i are data points at parameter value x_i and $f(x_i)$ are the respective values computed by the model. χ^2 is then the sum of the squared mismatch between model and data, normalized by the uncertainty ϵ_i which can be for instance the standard deviation in experimental data. In the case here, the data consists of production curve $Q(t)$, pressure drop Δp, and saturation profiles $S_w(x,t)$.

3. Algorithm and implementation

A key element of the methodology used here is the numerical flow model and relative permeability and capillary pressure parameterizations which solved numerically with a 1D native Python code that is accelerated with the `numba` just-in-time compiler.

3.1. Flow Solver Implementation in native Python

The computational domain was a 1D linear grid consisting of n_x (typically $n_x = 50$) grid blocks in x direction as sketched in Figure 3. At the inlet the water phase was injected at flow rate q_{in}. For the grid blocks in the physical grid, the respective flow parameters (porosity ϕ, permeability K, relative permeability $k_{r,\alpha}\ (S_w)$ and capillary pressure $p_c\ (S_w)$ saturation functions were defined. Note that the $k_{r,\alpha}\ (S_w)$ and $p_c\ (S_w)$ models from eq. (8)-(10) were not hard-coded in the solver, first converted into a cubic spline interpolation which was then used in the solver. That provides additional flexibility to change the model using e.g. the Chierici model for relative permeability (Valdez et al. 2020) or using a direct spline- or NURBS model (Manasipov, R., Jenei 2020).

Also, initial conditions in terms of saturation ($S_{w,i}$) were defined. At the inlet, there was a constant flow boundary conditions and at the outlet constant pressure was applied. In addition, a capillary pressure $p_c = 0$ boundary condition was applied which then caused the capillary end-effect (Huang & Honarpour 1998).

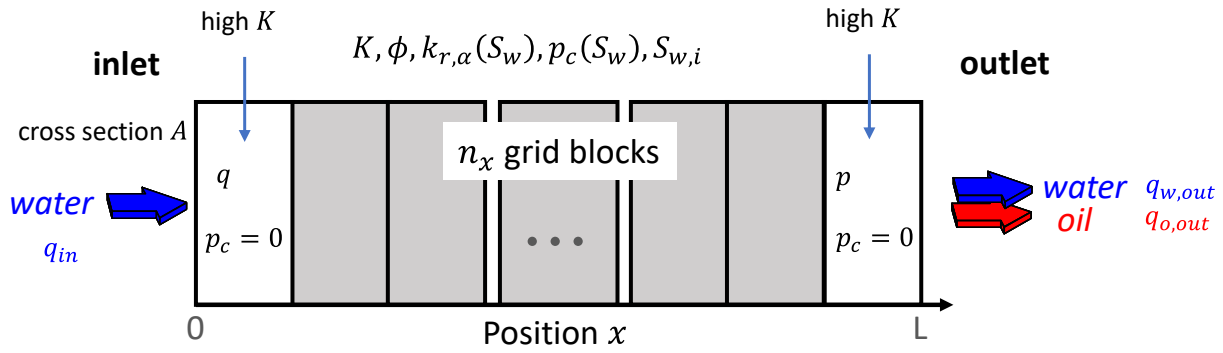

Figure 3 Computation domain. A 1D linear grid is used with n_x grid blocks (typically $n_x = 50$) in x direction over the sample length L. At the inlet the water phase is injected at flow rate q_{in}. For the grid blocks in the domain the respective flow parameters (porosity ϕ, permeability K, relative permeability $k_{r,\alpha}(S_w)$ and capillary pressure $p_c(S_w)$ saturation functions need to be defined. Also, the initial conditions need to be defined particularly in terms of saturation ($S_{w,i}$). At the inlet we apply constant flow boundary conditions and at the outlet constant pressure. In addition, a capillary pressure $p_c = 0$ boundary condition is applied (Huang & Honarpour 1998).

The rock and fluid properties were defined in a set of variables (which are the ones used for the ground-truth in this work) as described in Appendix A.1.1 which are then used in the displacement model A.1.2

The numerical solver was a 1D explicit finite difference scheme with time stepping control. It handled two-phase incompressible flow with capillarity and gravity in unidirectional flow. It cannot handle counter-current imbibition. The solver was contained in the `displacementmodel1D2P001.py` library and uses the `numba` just-in-time-compiler for speedup. A code example is given in Appendix A.1.3

A typical relative permeability simulation with a domain size with $n_x = 50$ took about 50 ms which was about a factor of 400 faster than calling an external reservoir simulator through a wrapper, mainly because external simulators have an initialization period before each run on a second time scale.

The flow solver then runs over a pre-defined schedule where flow rates and fractional flows were defined

```
#times in min, injrate in cm3/min

Schedule = pd.DataFrame(
     [[0.0,    0.1, 1.0],
      [1.4,  2*0.1, 1.0],      # bump floods
      [1.6,  5*0.1, 1.0],
      [1.8,  10*0.1, 1.0]],    # bump floods
    columns=['StartTime','InjRate','FracFlow'] )
```

3.2. Solver Convergence

The solver convergence was tested for the steady-state mode example "SS-Sample1-HS-01" in Sorop et al. 2015. The respective Newton iterations and time step size are displayed in Figure 4.

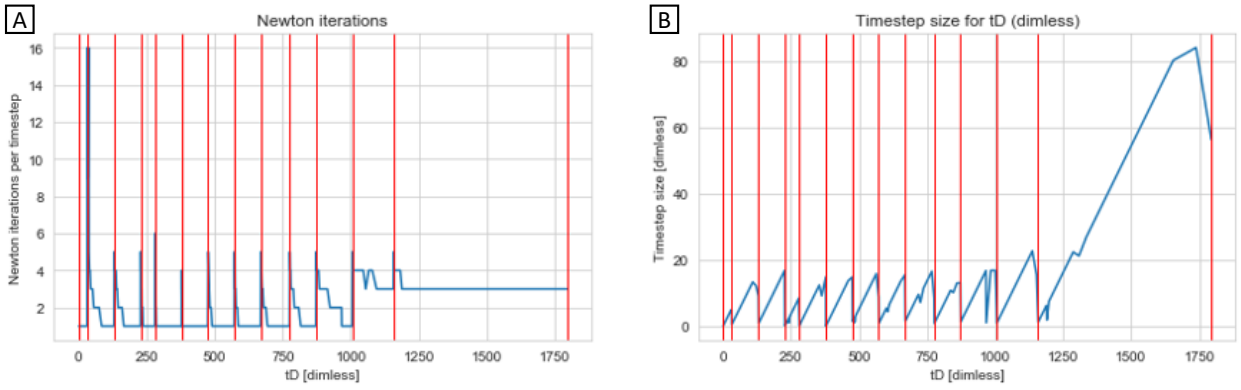

Figure 4 Solver convergence: Newton iterations (A) and time step size (B) for the steady-state example "SS-Sample1-HS-01" in Sorop et al. 2015.

3.3. Validation of the Flow Simulator

The 1D Python code used in this work was validated against the solver benchmark in the Lenormand et al. 2016 work. The validation was done specifically for using $N_x = 100$ grid blocks and adjusting the time step size such that $\delta S_w < 0.01$ at each time step, to be consistent with the benchmark example.

In the Lenormand et al. 2016 publication, 5 solver benchmarks were defined. Here we use case 1-4 as validation. Case 1 is a steady-state (SS) situation with a smooth $p_c(S_w)$ curve, case 2 is a steady-state situation with a sharp $p_c(S_w)$ curve, case 3 is an unsteady-state (USS) case with sharp $p_c(S_w)$ curve, and case 4 is an unsteady-state situation with $p_c = 0$ (Buckley-Leverett). As shown in Figure 5, for all 4 cases we find excellent agreement of the 1D-Python code presented in this work and the reference from Lenormand et al. 2016 in terms of pressure drop and production curve.

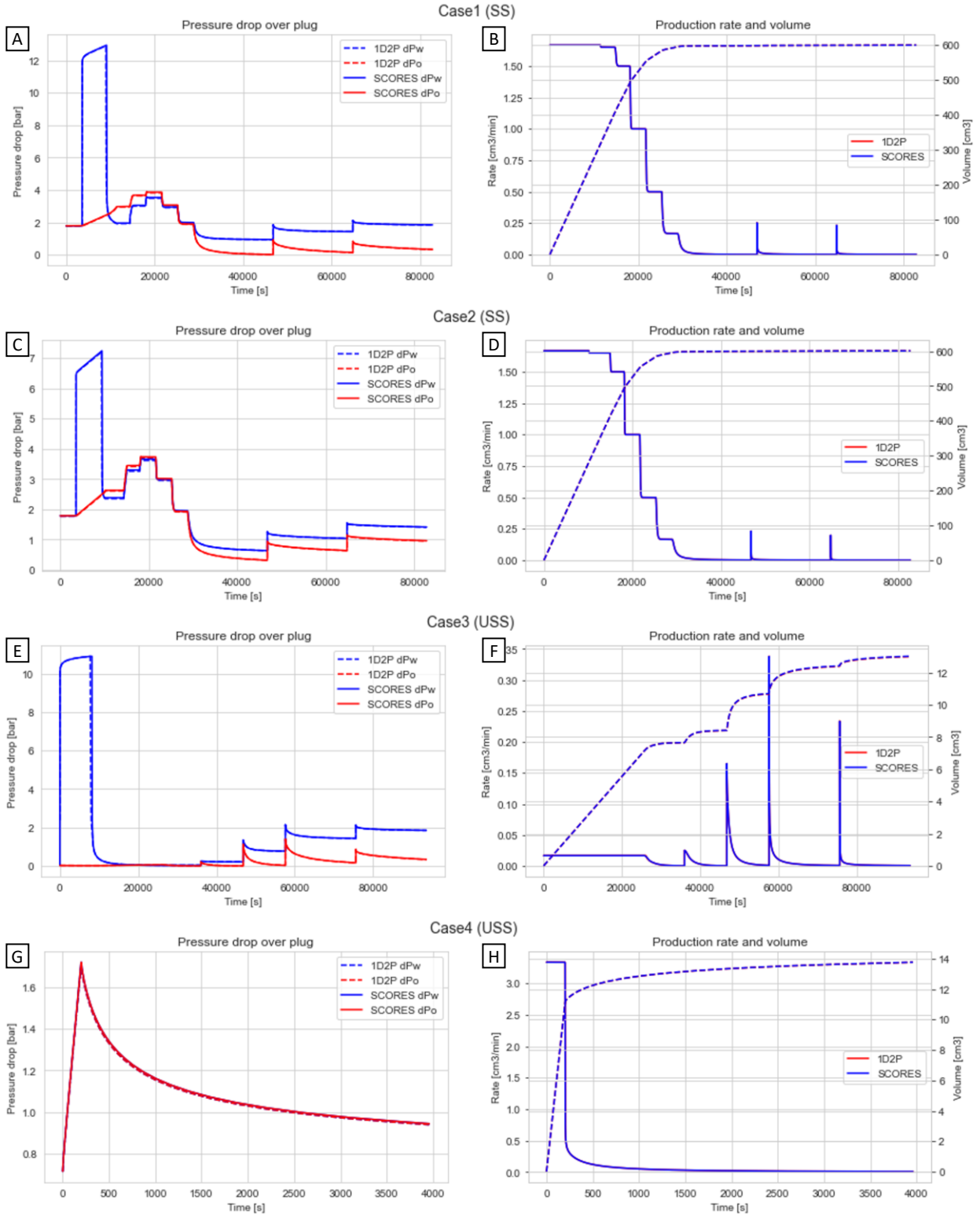

Figure 5 Validation of the 1D Python code against the solver benchmark cases 1-4 in Lenormand et al. 2016. Case 1 (A,B) is a steady-state (SS) situation with a smooth $p_c(S_w)$ curve, case 2 (C,D) is a steady-state situation with a sharp $p_c(S_w)$ curve, case 3 (E,F) is an unsteady-state (USS) case with sharp $p_c(S_w)$ curve, and case 4 (G,H) is an unsteady-state

situation with $p_c = 0$ (Buckley-Leverett). For all 4 cases we find excellent agreement of the 1D-Python code presented in this work and the reference from Lenormand et al. 2016 in terms of pressure drop and production curve.

3.4. Objective function

Production data Q_i, pressure drop Δp for water and oil phases, and saturation S_w of the reference data set (index ref) were incorporated in the objective function by adding the individual terms

$$\chi^2 = w_Q \sum_{t_i} \frac{\left(Q_{nw,i} - Q_{nw,i}^{ref}\right)^2}{\delta Q_i^2} + w_p \sum_{t_i} \frac{\left(\Delta p_i - \Delta p_i^{ref}\right)^2}{\delta p_i^2} + w_S \sum_{x_i} \frac{\left(\mathrm{S_{w,i}} - S_{w,i}^{ref}\right)^2}{\delta S_{w,i}^2} \quad (12)$$

with weighting factors w_Q, w_p and w_S for production data, pressure drop and saturation profiles, respectively. While normalization by the standard deviation associated with each data set already provided a normalization in terms of magnitude of individual values, the weight of data in the objective function still depended on the number of data points. When incorporating production curve and pressure drop, these were averaged over the domain in x and tabulated for times t_i. However, saturation data were not averaged and, hence, were the number of points in time multiplied by the number of sampled points in space; they had a larger weight. However, not all saturation profiles could be included in the objective function for an number of reasons. Therefore, these weighting factors w_Q=`op_weight`, w_p=`dp_weight` and w_s=`sw_weight` were left to be user-specified when defining the objective function. A code example is given in Appendix A.1.4

3.5. Optimization: Levenberg-Marquardt implementation in `lmfit`

In order to minimize the cost function< χ^2 we used the gradient-based Levenberg-Marquardt (Levenberg 1944, Marquardt 1963) implemented in the Python `lmfit` package (Newville et al. 2014). From the `lmfit` package, we used the `minimizer` function which minimized the objective function. Note that, the χ^2 from eq. (11) was computed by the minimizer itself, where the $\frac{y_i - f(x_i)}{\epsilon_i^2}$ vector was passed to the minimizer.

In the `lmfit` package the Jacobian i.e. the gradients of χ^2 with respect to varied model parameters, was automatically computed numerically in the background.

For each fit parameter an initial value was defined, the bounds consisting of minimum and maximum values (which could be, to a certain extent, guessed by physically meaningful ranges, e.g. $0.03 \leq S_{w,c} \leq 0.2$ and $0.05 \leq S_{n,r} \leq 0.40$) and whether the parameter was varied during the χ^2 minimization. The `params_pckr` object contained respective parameters (Table 1).

Table 1. List of optimization parameters used in Levenberg-Marquardt implementation

Name	Value	Min	Max	Stderr	Vary
Eo	3.475	0.0001	50	None	True
Ew	2.781	0.0001	50	None	True
Lo	1.819	1.5	5	None	True
Lw	1.601	1.5	5	None	True
Sorw	0.1399	0.05	0.40	None	True
Swc	0.08	0.03	0.20	None	False
Swi	0.13	0.1	0.3	None	True
To	1.012	1	5	None	True
Tw	1.055	1	5	None	True
aoi	0.9	0.45	2.7	None	True
awi	0.3	0.15	0.9	None	True
ci	0	0	0.22	None	True
cwi	0.011	0.0022	0.022	None	True
kroe	1.01	0.05	1.1	None	True
krwe	0.6775	0.05	1.1	None	True

The χ^2 minimization is then executed by calling the `minimizer` function with the objective function `uss_matchobj` and the fit parameter object `params_pckr`

via the command `result_pckr = Minimizer(uss_matchobj, params_pckr).least_squares(diff_step=1e-4,verbose=2)`

The χ^2 minimization typically converges between 20 and 100 iterations which takes between approximately 10 and 60 s.

3.6. Optimization: Markov-chain Monte Carlo implementation in `emcee`

Since for the problem of interest non-uniqueness is possible or even expected, i.e., the χ^2 landscape can exhibit multiple minima (Berg et al. 2020), the gradient-based optimization can converge to different minima i.e., result in

different outcomes depending on the starting point. In order to be robust against that, a Markov-chain Monte Carlo approach was used to double-check. Here, we used the `emcee` package (Foreman-Mackey et al. 2012) which was a native Python implementation and had the convenience of being callable directly through `lmfit` i.e., using the exactly the same model and cost function implementation as for the gradient-based optimization. A code example is given in Appendix A.1.5

4. Results

4.1. Ground-Truth Generation: Single-rate

A ground-truth data set was generated starting with defining a set of relative permeability and capillary pressure-saturation functions. For the relative permeability and capillary pressure relations, Corey and Skaeveland models were used, respectively. Then 10% noise was added, and respective production curve, pressure drop, and saturation profiles were computed numerically by solving the flow model, to which a further 10% random noise was added. The result is displayed in Figure 6.

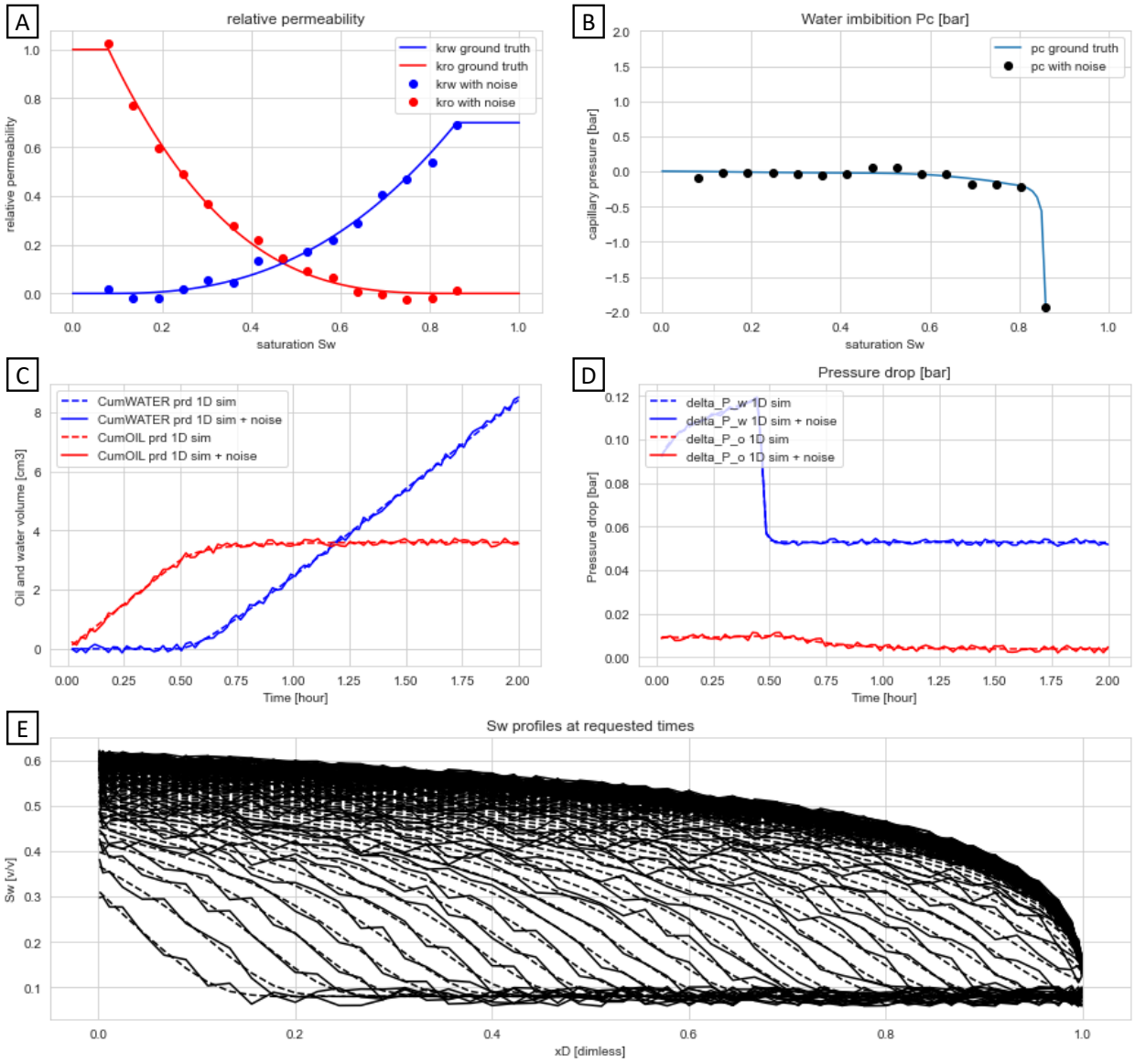

Figure 6 Generation of a ground-truth data set starts with defining a set of relative permeability (A) and capillary pressure-saturation functions (B). Then 10% noise was added, and respective production curve (C), pressure drop (D) and saturation profiles (E) were computed, to which again 10% random noise was added (in the saturation profiles the dotted lines represent the output of the flow model for (A) and (B) without the extra 10% noise). Note that for the saturation profiles the position x has been normalized by the sample length L i.e. $x_D = x/L$. The flow is from left to right. Clearly visible is the capillary dispersion zone i.e. the shock front is not straight but smeared out by capillarity (Lake, 1984) and the capillary end-effect (Huang & Honarpour 1998) at the outlet side.

It is important to point out here that the ground-truth was constructed such that

- There was a clearly notable capillary-end effect i.e., a saturation gradient a the outlet side (Huang & Honarpour 1998)
- There was a capillary dispersion zone i.e., the shock front was smeared out by capillarity as sketched in Figure 7 (Lake 1984) which was on the one hand well resolved by the saturation measurement but small compared with the sample length.

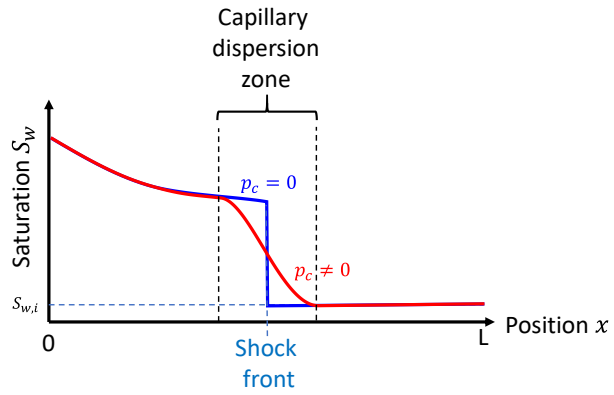

Figure 7 Buckley-Leverett profile with a sharp shock front for $p_c = 0$ and a wider capillary dispersion zone for $p_c \neq 0$.

Both aspects are important because in this way, during inverse modelling there is a sensitivity of features in the experimental data that are sensitive to the capillary pressure-saturation function $p_c(S_w)$ independently of pressure drop and production curve.

Also note that here both the oil and water pressure were used. In real experiments, these are not independently accessible. In practice, only the pressure of the mobile phase is accessible, which is essentially the pressure of the more mobile phase which is in most cases the water phase.

4.2. Match varying both relative permeability and capillary pressure

In the first step, the synthetic data set from Figure 6 was matched by varying both relative permeability and capillary pressure. The residual oil saturation was also varied. For relative permeability the LET parameterization was used. The parameters E_w, E_o, T_w and T_o of the LET model were kept fixed which made it practically equivalent to a Corey model. The saturation profiles were not considered in the objective function χ^2.

As shown in Figure 8 there was a very good match for pressure drop and production curve, and the saturation profiles showed a very good match even though they were not part of the objective function.

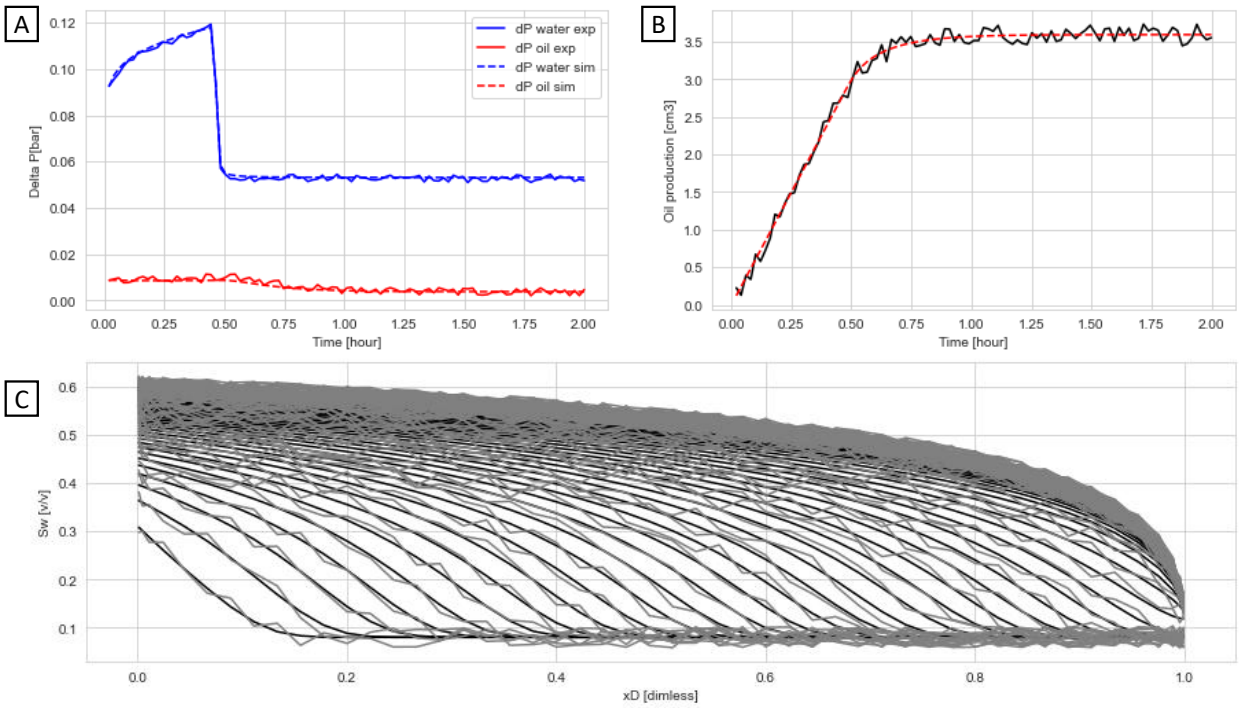

Figure 8 Match of the flow model to the synthetic data set from Figure 6. In the match both relative permeability and capillary pressure very varied, including residual oil saturation. The saturation profiles were not considered in the objective function. A very good match was observed for pressure drop (A), production curve (B) and also for the saturation profiles (C) even though they were not part of the objective function.

However, even though the match in terms of pressure drop, production curve and saturation profiles were almost perfect, the resulting relative permeability was significantly different from the ground-truth as shown in Figure 9. Why such a difference was possible, became more obvious when the uncertainty ranges were considered for relative permeability that are estimated from the covariance matrix of the least-squares fit (Berg et al. 2020, Berg et al.

2021), shown in Figure 9C. The uncertainty ranges were significant and covered essentially the difference between the match and the ground-truth.

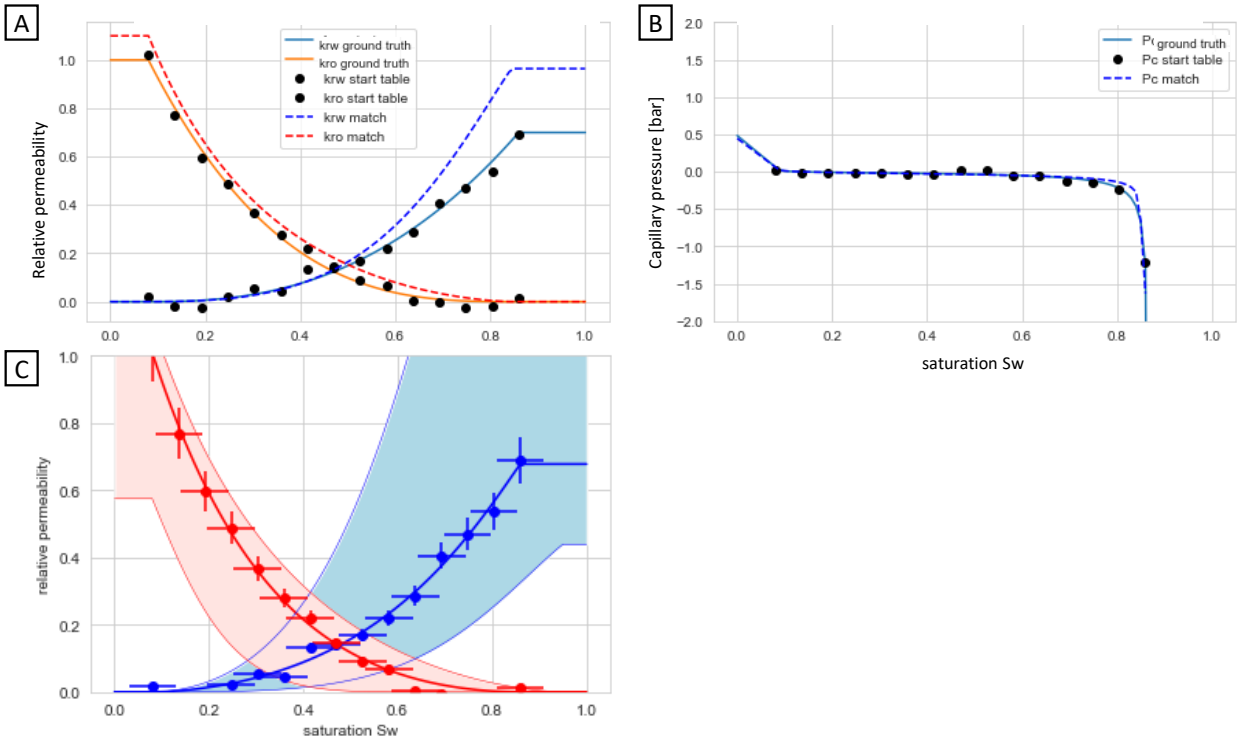

Figure 9 Relative permeability (A) and capillary pressure-saturation functions (B) for the match from Figure 8. Even though the match in terms of pressure drop, production curve and saturation profiles is almost perfect, the ground-truth in terms of relative permeability is not recovered. Instead, there are notable differences, which become even more obvious when considering the uncertainty ranges (C) which are obtained from the covariance matrix and marked as shaded regions.

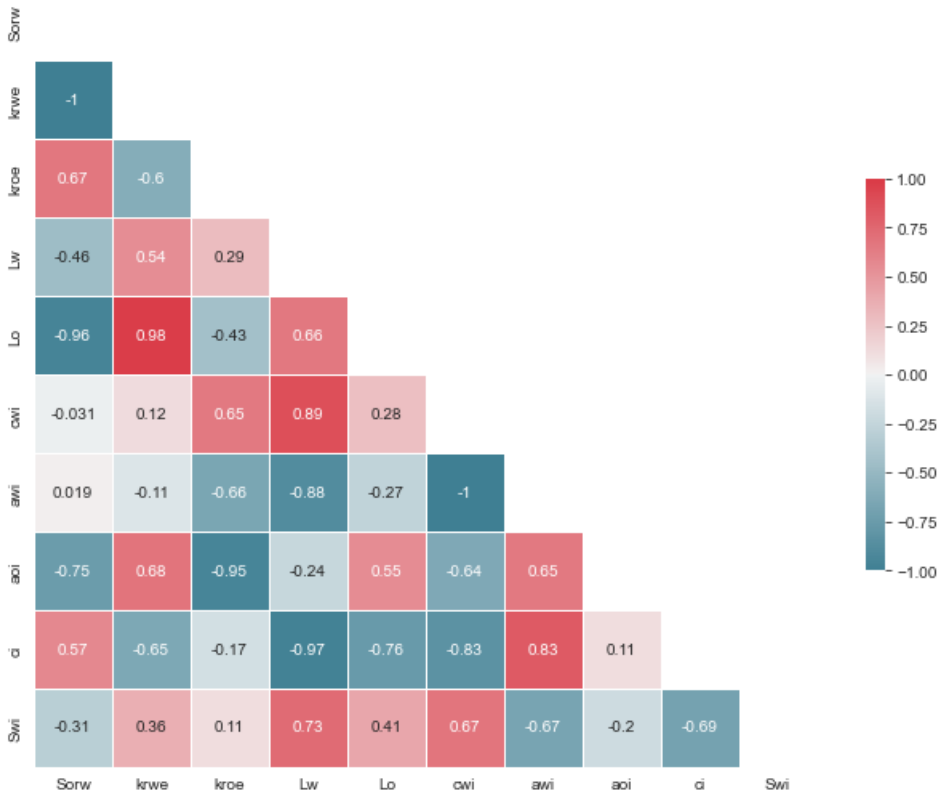

Figure 10 Cross-correlation between model parameters employed in the fit from Figure 8 and Figure 9. Many cases of strong correlation (or anti-correlation) suggest that the problem is either over-parameterized or under-constrained.

The large uncertainty ranges for relative permeability in Figure 9C were consistent with many cases of strong correlation between fit parameters as shown in Figure 10.

The uncertainty ranges of relative permeability and cross correlations of model fit parameters obtained from the least squares fit were overall consistent with the error ellipses computed by MCMC using 20000 iterations, displayed in Figure 11. That suggested that the model was either over-parameterized (which meant that we would need to fix e.g., capillary pressure) or under-constrained. The latter would imply that there was need to invoke more experimental data such as saturation profiles in the objective function.

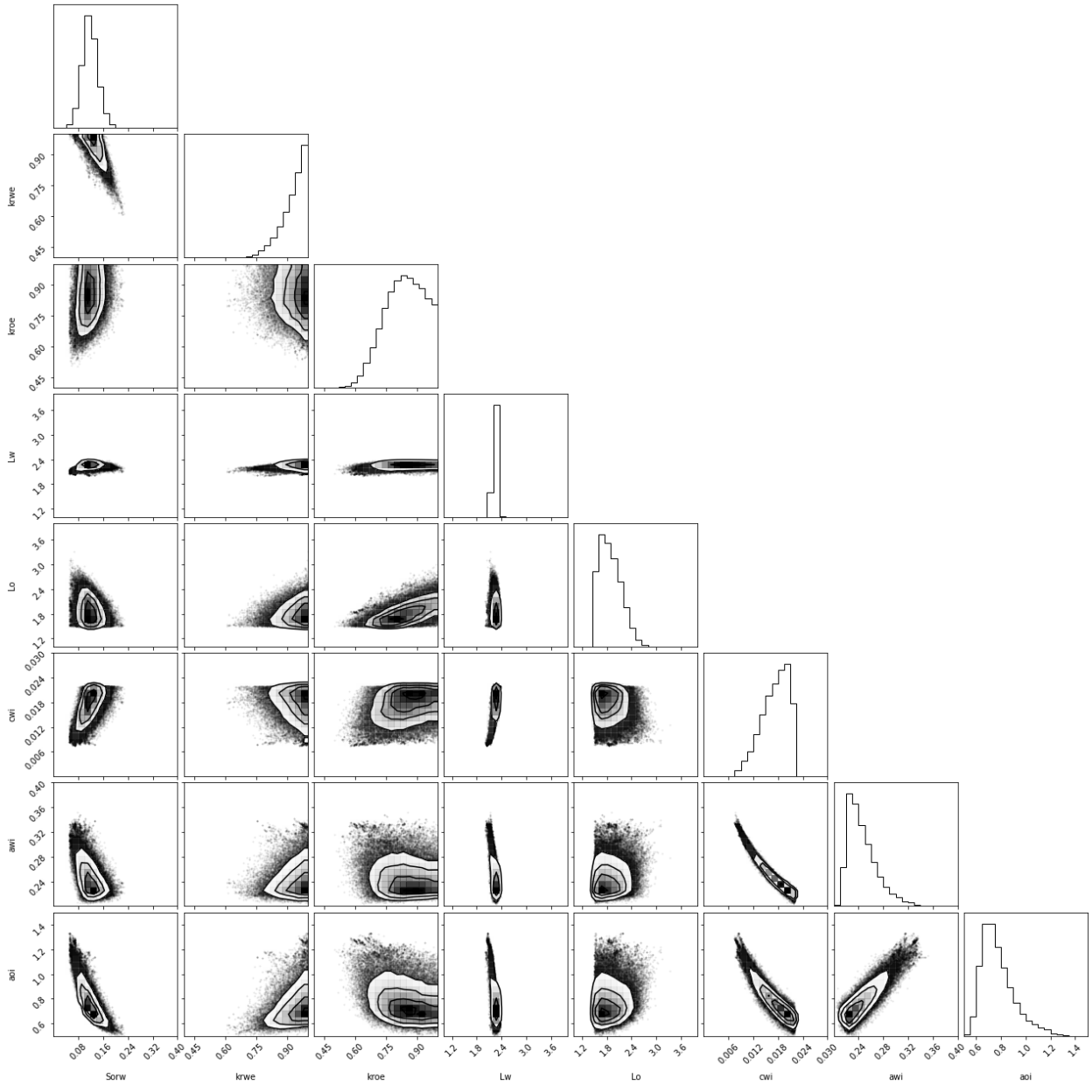

Figure 11 Error ellipses for the case from Figure 8 and Figure 9 but computed by MCMC (20000 iterations).

4.3. Including Saturation Profiles $S_w(x)$ in the Objective Function

In the next step, 11 saturation profiles $S_w(x)$ were included in the objective function. The results of the match are shown in Figure 12. The quality of the match was overall of similar quality as the one shown in Figure 8 where no saturation profiles were considered in the objective function. However, the uncertainty ranges for relative

permeability notably decreased as shown in Figure 13 and the associated cross-correlations between model fit parameters also decreased notably, as shown in Figure 14. Also the error ellipses obtained by MCMC were significantly smaller (Figure 15) compared with the case where no saturation profiles were considered in the objective function (Figure 11). That demonstrated the value of including saturation profiles $S_w(x)$ into the objective function in a very visual way.

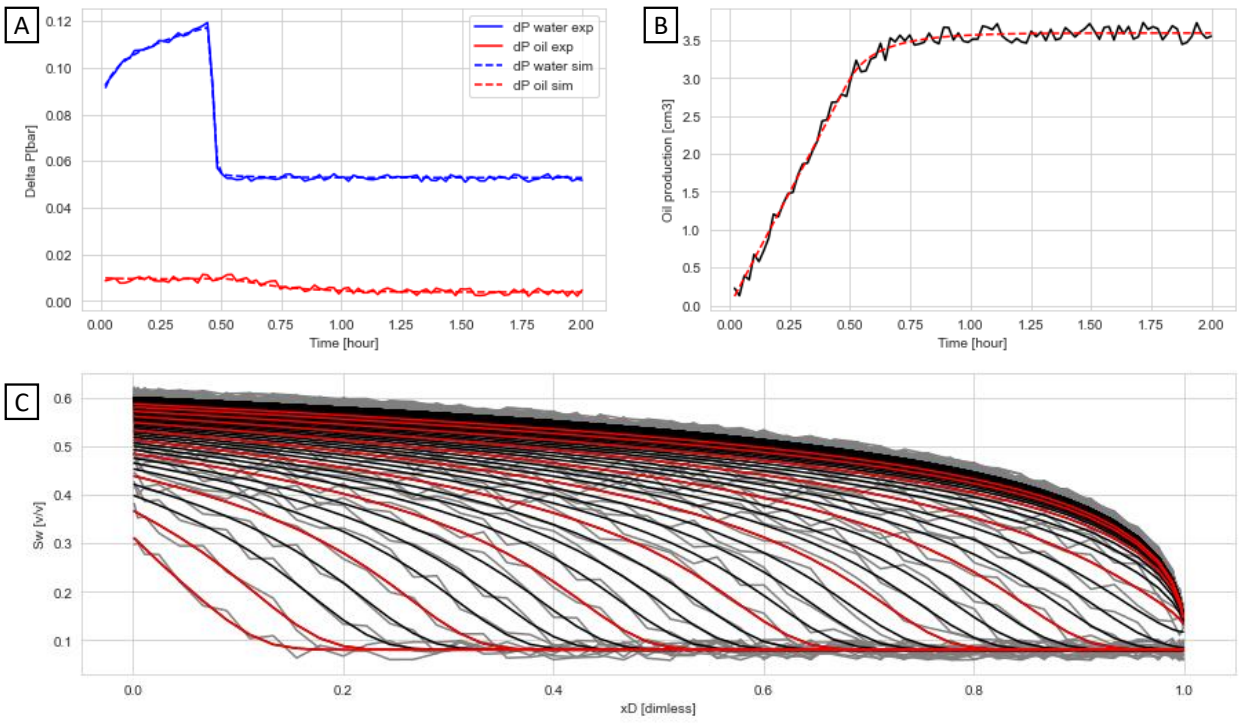

Figure 12 Match of the flow model to the synthetic data set from Figure 6. In the match both relative permeability and capillary pressure very varied, including residual oil saturation. 11 saturation profiles (C) were included in the objective function (shown in red). A very good match was observed for pressure drop (A), production curve (B) and also for the saturation profiles (C) but overall similar quality as in the match in in Figure 8 where no saturation profiles were considered in the objective function.

However, uncertainty ranges of relative permeability were still large; there were also still several model fit parameter pairs with strong cross-correlations. That suggested that the model was still not sufficiently constrained, and potentially more experimental data was needed.

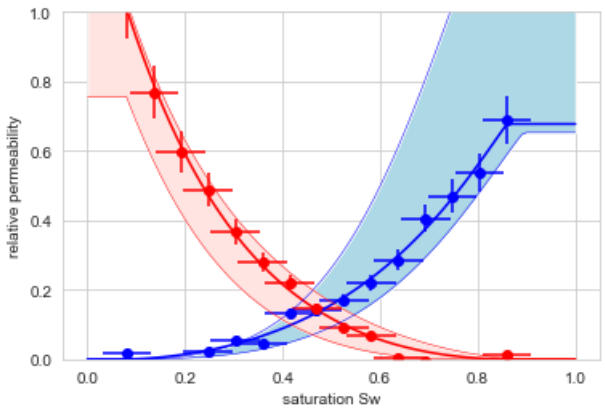

Figure 13 Relative permeability uncertainty ranges for the match from Figure 12 where 11 saturation profiles had been considered in the objective function. The uncertainty ranges notably decreased compared to the case without saturation profiles in the objective function, shown in Figure 9C.

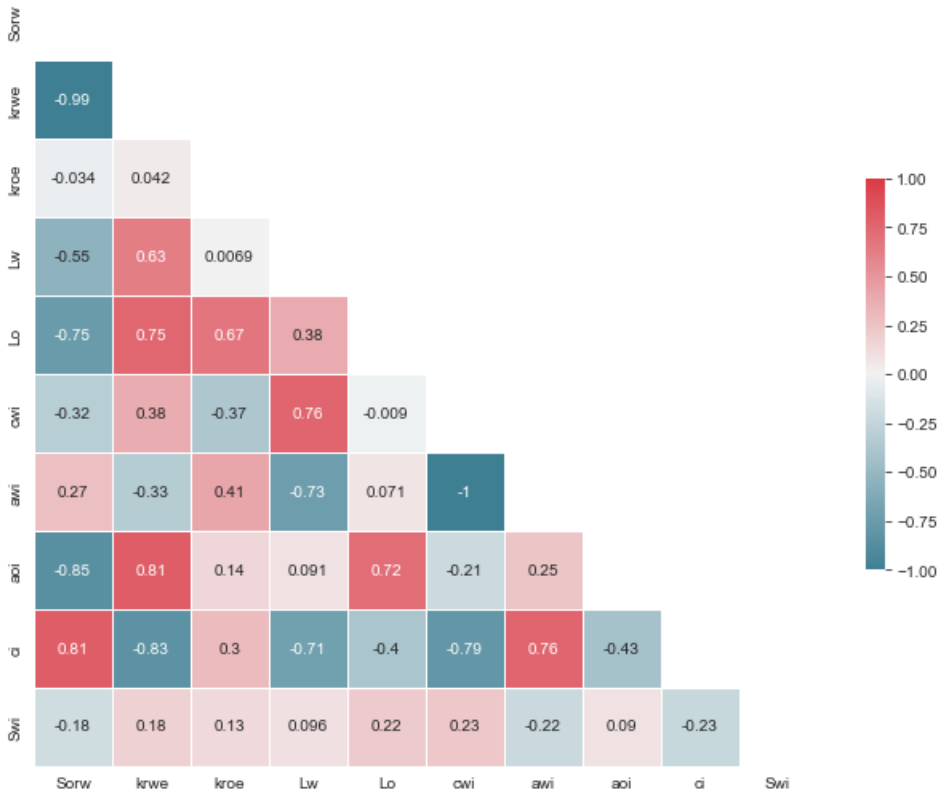

Figure 14 Cross-correlation between model parameters employed in the fit from Figure 12 and Figure 13. Compared with the case without saturation profiles in the objective function (Figure 10), the cross correlations significantly decreased, but are still considerably large for several parameter pairs.

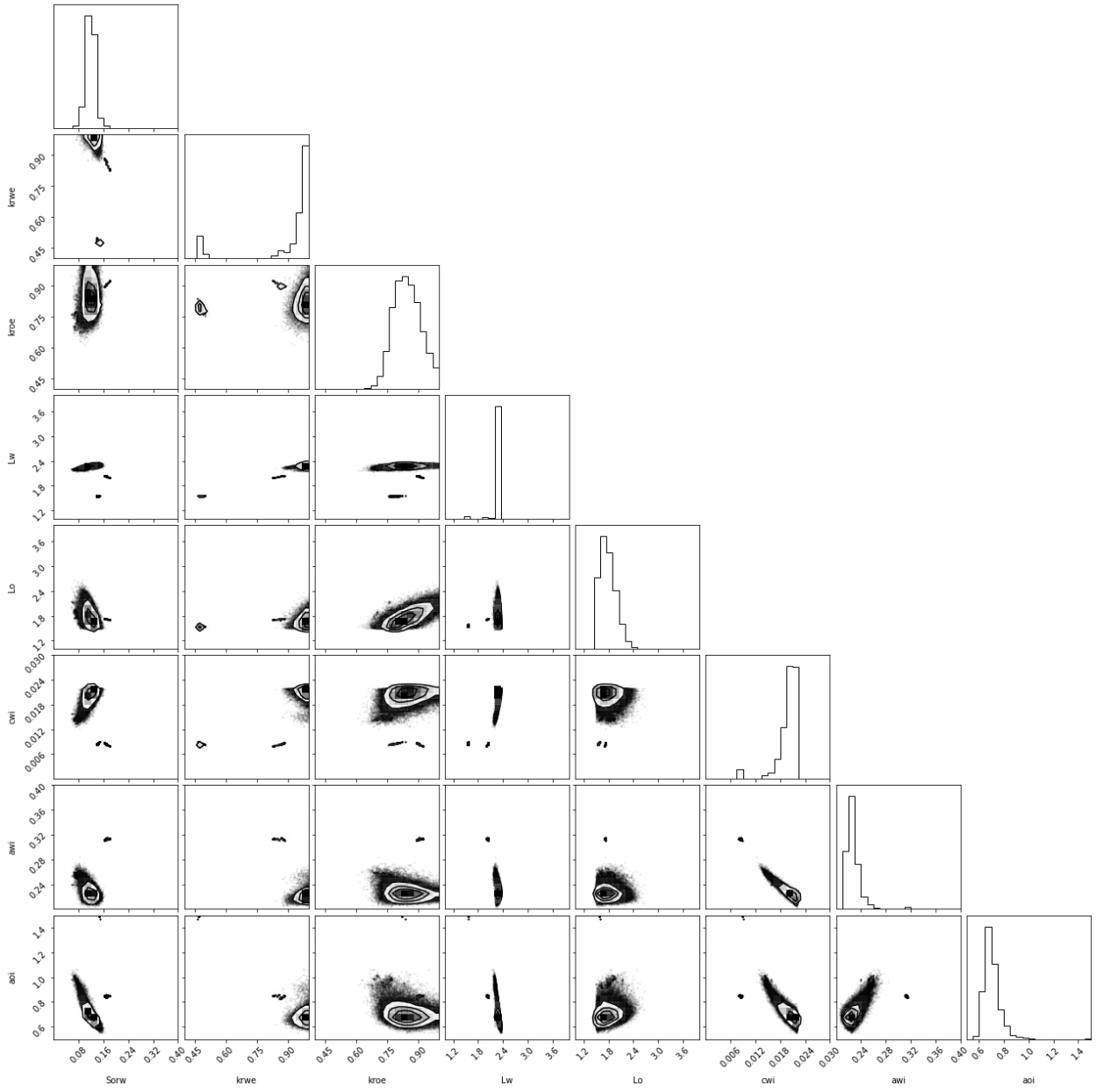

Figure 15 Error ellipses for the case from Figure 12 and Figure 13 but computed by MCMC (20000 iterations). Similar as the reduction of uncertainty ranges for relative permeability (Figure 9C vs. Figure 13) and reduction of cross correlations from the least squares fit (Figure 10 vs. Figure 14) by incorporating 11 saturation profiles the error ellipses significantly shrink compared with the case where no saturation profiles were considered in the objective function (Figure 11).

4.4. Including a Multi-Rate "Bump Flood"

In the next step, a multi-rate "bump flood" was added to the synthetic data set where flow rate was increased in three steps by 2x, 5x and 10x (Masalmeh et al. 2014). In addition, 8 more saturation profiles were included in the objective function, distributed over the three additional flow rates. The results shown in Figure 16 show a very good match with all parameters.

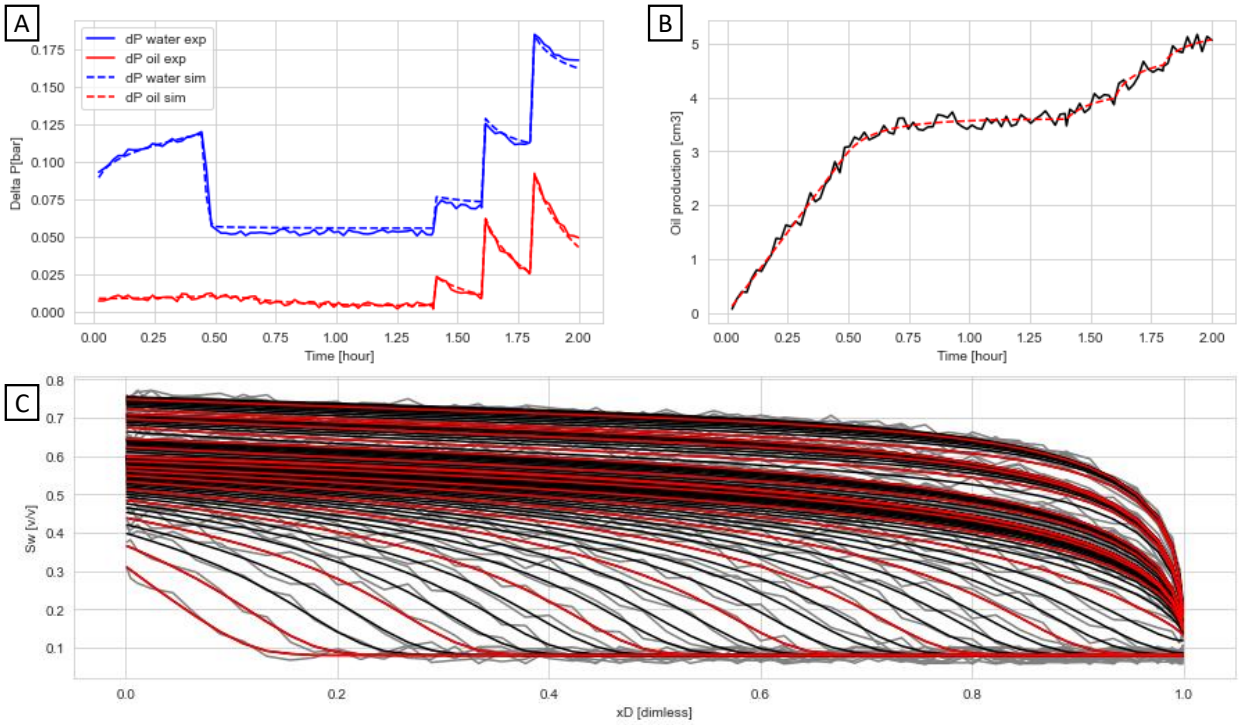

Figure 16 Match of the flow model to the synthetic data set from Figure 6 adding 3 additional flow rate steps where the flow rate is increased by 2x, 5x and 10x. In the match both relative permeability and capillary pressure very varied, including residual oil saturation. 19 saturation profiles (C) were included in the objective function (shown in red). A very good match was observed for all parameters.

Due to the bump floods, the uncertainty range for the resulting relative permeability now significantly decreased as shown in Figure 17. The match was consistent with the ground-truth within the range of added noise. Similarly, the capillary pressure saturation function also converged to the ground-truth, except for a minimal difference in residual oil saturation. Most importantly, the uncertainty ranges for relative permeability were now similar as the added noise. This suggested an overall large degree of consistency and suggested that, indeed, the set of experimental data used (i.e. saturation profiles and multi-rate bump floods) were sufficient to constrain the match.

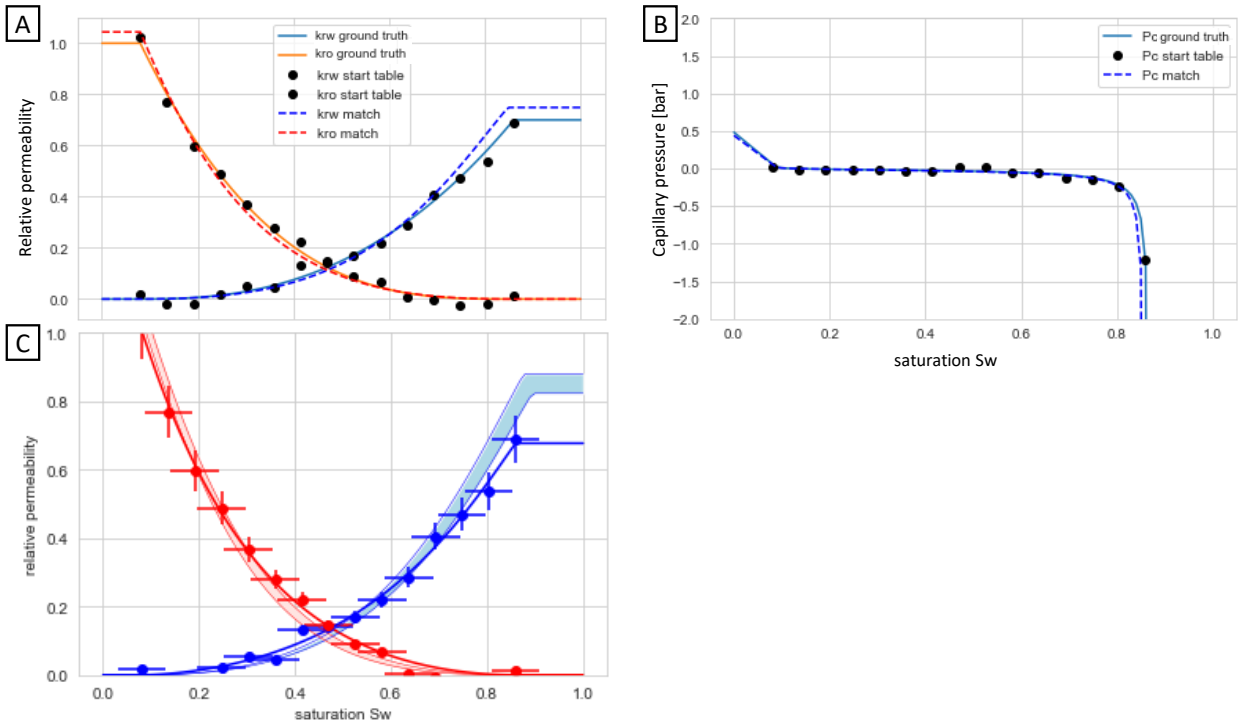

Figure 17 Relative permeability and capillary pressure function of the match for the match from *Figure 16* where 3 bump floods and 19 saturation profiles had been considered in the objective function. The match is now very close to the ground truth. By including the bump floods, relative permeability uncertainty ranges have significantly decreased compared with the two cases without bump floods (Figure 9C and Figure 13) and are now overall in the range of the added noise.

Also, the cross correlations of fit parameters overall further decreased as shown in Figure 18. However, in comparison to the cross correlations observed before the bump flood (Figure 14) for some parameter pairs, the cross correlation actually increased. That means that even though the convergence of relative permeability against the ground-truth, the cross correlations for some parameter pairs very substantial indicating that the model was still not entirely sufficiently constrained by the data.

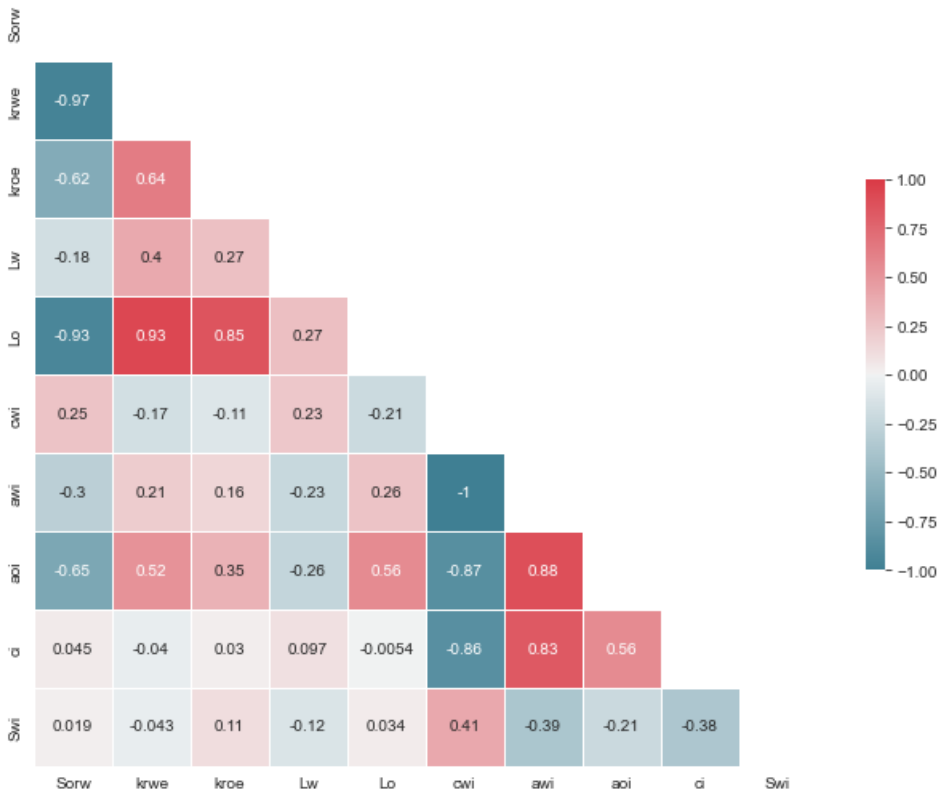

Figure 18 Cross-correlation between model parameters employed in the fit from Figure 16 and Figure 17. Overall, the cross correlations further decreased compared with the cases without bump flood (Figure 10 and Figure 14). But there are cases where cross correlations increased.

4.5. Considering only Effective Pressure Drop (instead of both Oil and Water Pressure Drop)

As already stated in the section where the ground-truth was constructed, so far, we operated with both oil and water pressure drop. However, in experiments these are generally not independently accessible. Therefore, here, we assessed how significant the impact would be when only an effective pressure drop is used, the oil pressure drop before the water breakthrough and the water pressure drop after breakthrough (i.e. effectively we operate mainly with the water pressure drop). that the results showed that there was very little impact on relative permeability and capillary pressure, as shown in Figure 19. They were essentially identical within the uncertainty range compared with the situation where both water and oil pressure drop were considered in the objective function (Figure 17).

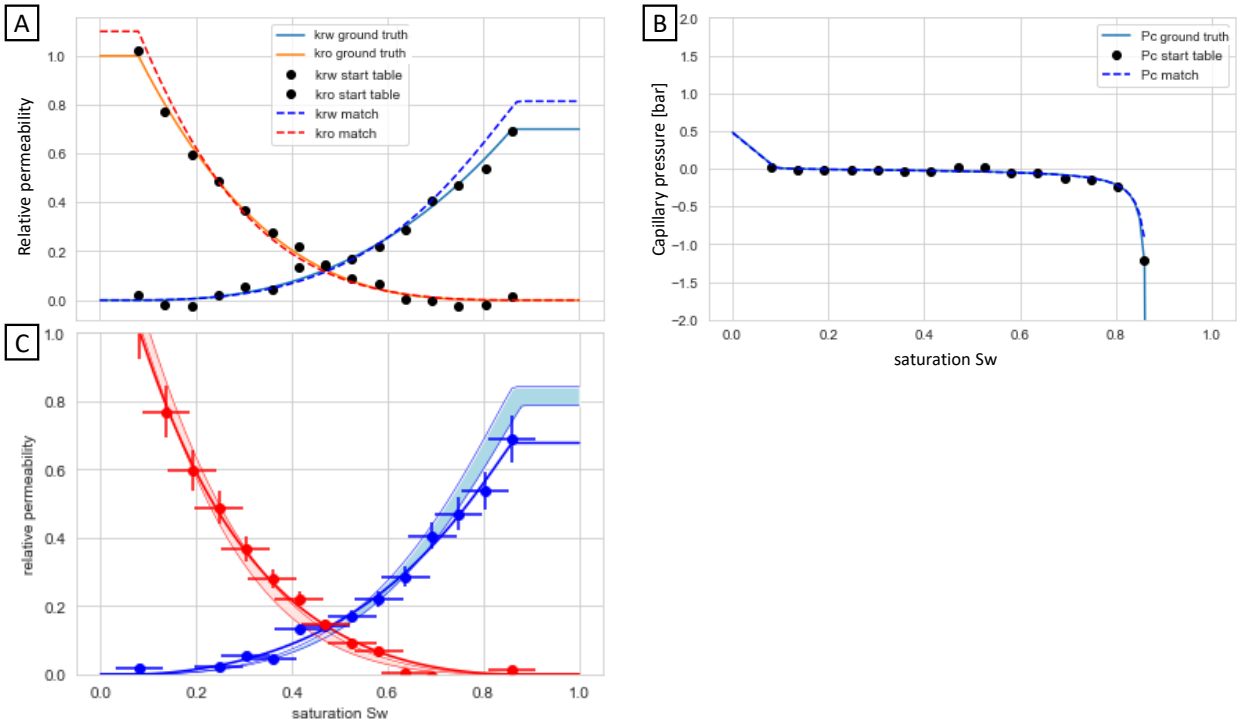

553

554 *Figure 19* Relative permeability and capillary pressure function considering 3 bump floods and 19 saturation profiles in the
555 objective function but matching only the effective pressure drop and not water and oil pressure drop independently
556 (because these are in most experiments not independently accessible). The results are very similar to the case where both
557 water and oil pressure drop are used (Figure 17) i.e. identical within the uncertainty.

558

559

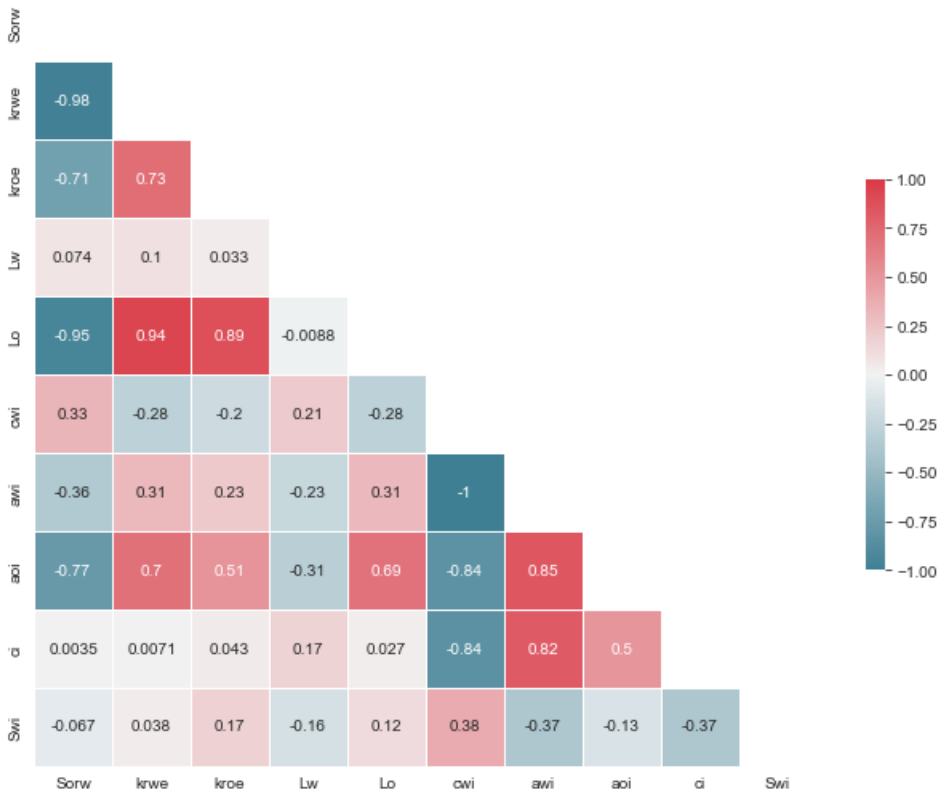

Figure 20 Cross-correlation between model parameters employed in the fit from Figure 19 where only one effective pressure drop has been considered which reflects the experimental reality in most cases. Compared with the situation where both water and oil pressure drops were considered as independent parameters in the objective function (Figure 18), the correlations are very comparable.

4.6. Poorly resolved capillary dispersion zone

In the next step, we considered a situation where the capillary dispersion zone was poorly resolved. We started with the same ground-truth as before but increased the capillary pressure by a factor of 10 (Figure 21B) and decreased the length of the core by a factor of 2. For these conditions, the capillary dispersion zone (see sketch in Figure 7) was only poorly resolved in the computational domain as shown in Figure 21C. Consequently, the uncertainty range for relative permeability increased significantly (Figure 21D) compared with the reference case from Figure 19C. It was almost at the level of Figure 9C where no saturation profiles were considered in the objective function and no bump flood was performed.

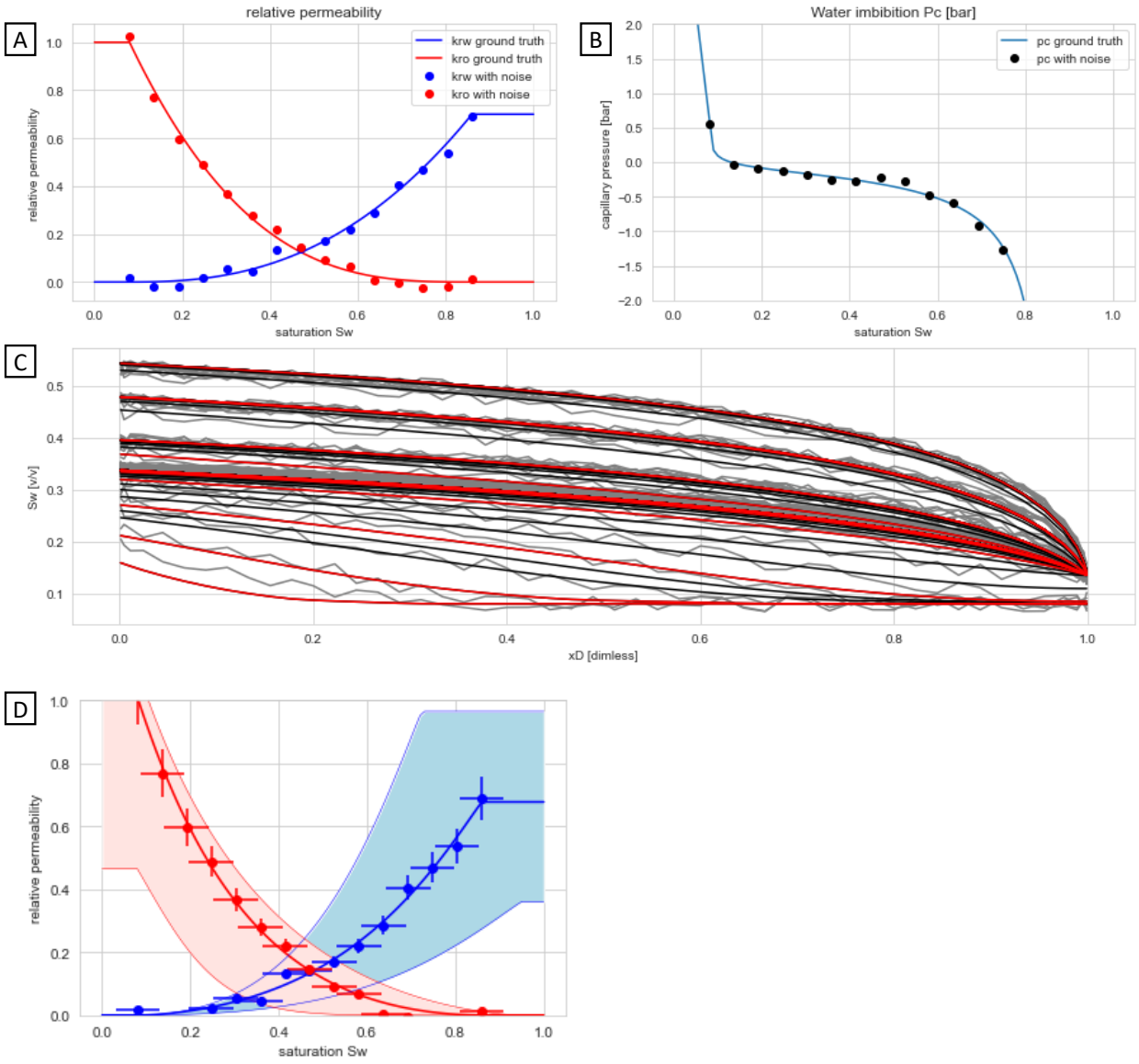

576

577 *Figure 21* Modified ground-truth where the relative permeability (A) is kept the same as in the previous cases but the capillary
578 pressure (B) is increased by a factor 10 compared with the ground-truth from Figure 6. Also the length of the core is
579 reduced by half. As a consequence, the capillary dispersion zone (Figure 7) is poorly resolved over the length of the
580 sample. As a consequence, the uncertainty range for relative permeability significantly increases compared with Figure
581 19C.

582

583

5. Conclusions

In summary, we have addressed the question under which conditions relative permeability and capillary pressure could be obtained simultaneously from one single unsteady-state core flooding experiment. An inverse modelling workflow where a flow simulator was coupled with least-squares and Markov-chain Monte Carlo optimization tools was utilized. A synthetically created data set served as the ground-truth. We successively reduced the uncertainty ranges on relative permeability functions by systematically increasing the amount of (experimental) data to constrain the match. The findings are summarized in Figure 22. Using only production curve and pressure drop resulted in unacceptably large uncertainty ranges, which were the systematically decreased by including saturation profiles $S_w(x)$ into the objective function.

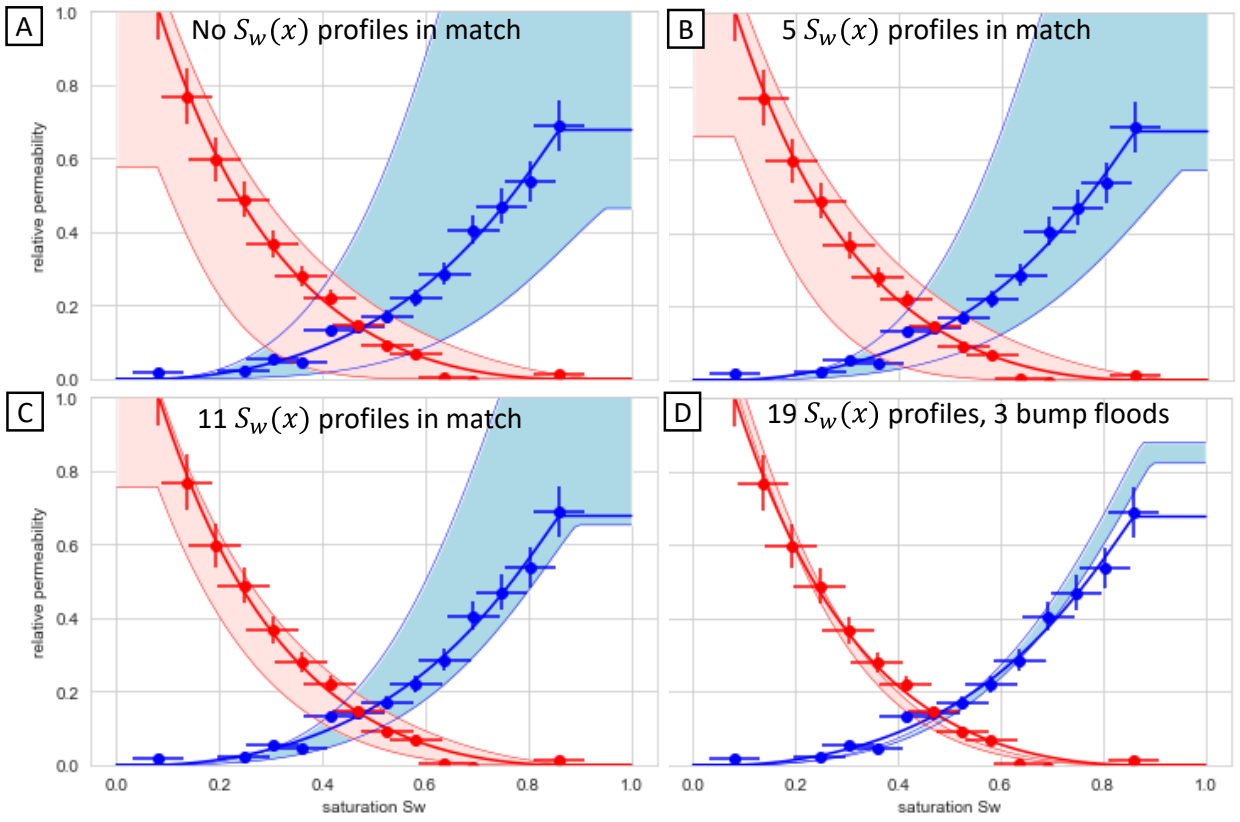

Figure 22 Relative permeability uncertainty ranges varying both relative permeability and capillary pressure-saturation functions for production curve and pressure drop only (A, see also Figure 9C), considering 5 saturation profiles (B, see also Figure 13) and 11 saturation profiles (C, see also Figure 13) and including 3 bump floods at 2x, 5x and 10x of the injection velocity (D, see also Figure 17). By including more experimental data to constrain the solution the uncertainty range systematically decreases, until it converges against the ground-truth (Figure 6A) within the uncertainty range of the added noise.

A really significant decrease in uncertainty ranges towards the range of the noise added to the ground-truth and convergence towards the ground-truth was achieved by including also three bump floods at 2x, 5x and 10x the flow rate.

While the analysis with a synthetic ground-truth data set is encouraging, there are several points that are important to consider. First, the correlation matrix in Figure 18 shows a large cross-correlations between fit parameters which suggests that model is either over-parameterized or under-constrained. Note that this model achieves self-consistency because parameterizations used for relative permeability and capillary pressure relations are compatible with the ones used in the ground-truth, i.e., there is a degree of self-consistency which may not be given for real experimental data. Furthermore, this scenario was chosen such that the capillary dispersion zone was relatively small compared with the sample length. For a scenario where the capillary dispersion zone is only poorly resolved, the uncertainty range of relative permeability significantly increases to similar levels where no saturation profiles were considered in the objective function and no bump floods were conducted. Also, in our well-behaved ground-truth scenario, several saturation profiles before breakthrough were accessible. In addition, the saturation profiles were available over the whole length of the sample including the capillary end-effect. These two conditions may not be given for experimental data because of limitations in e.g., scanning/image acquisition speed only 1 or 2 saturation profiles before breakthrough may be available and the scanning artefacts close to the sample end face may not fully resolve the capillary end-effect. That will lead to significant loss in fidelity of the match because this part of the data is of vital importance for constraining the match.

Therefore, ultimately this work concludes that under many practical conditions, it is not possible to obtain relative permeability and capillary pressure-saturation functions simultaneously from one unsteady-state experiment and the recommended practice for general-purpose special core analysis (SCAL) remains to determine relative permeability from steady-state experiments using an independently measured capillary pressure-saturation function (measured e.g. using the centrifuge method). Even though analytical interpretation methodologies may suggest this is possible, an assessment with the methodology presented here and using the numerical code made publicly available will allow to thoroughly assess and validate that. However, for situations where no steady-state measurements are possible or practical, e.g. for CO_2-sequestration, we also conclude that for specially-designed multi-rate unsteady-state experiments with cores that are long enough and scanning intervals short enough to capture several in-situ saturation profiles before breakthrough and fully resolving the capillary-end-effect, it is possible to determine relative

permeability within reasonable uncertainty ranges. The methodology presented here can be used to design and optimize such experiments and assess whether conditions are met to determine relative permeability and capillary pressure saturation functions simultaneously i.e., are both *output*, or whether an independently measured capillary pressure-saturation function is required as an *input*. However, it is also important to mention that core flooding experiments where gasses are involved include a range of phenomena such as phase behavior, mutual saturation of fluids, diffusive transport of gas and ripening dynamics (Berg et al. 2013, Berg et al. 2020a, Gao et al. 2021) which make CO_2 and H_2 experiments much more challenging and typically require much more through planning and more specialized setups than oil-brine immiscible cases. It is also worth mentioning that this inverse modelling concept hinges on the assumption that the 2-phase Darcy equation (1) is valid as it stands, i.e. holds equally well for steady-state and unsteady-state. We have to keep in mind that the 2-phase Darcy equation (1) has been introduced as a phenomenological extension to Darcy's law for single-phase flow without a rigorous fundamental basis. It has recently been shown that the 2-phase Darcy equation (1) can be derived from first principles for stationary situations i.e. steady-state based on the assumption that the collective energy dynamics of fluctuation terms averages out in a space & time average, while for non-stationary i.e. unsteady-state conditions this is not the case (McClure et al. 2022). What that exactly means for the practical difference between steady-state and unsteady-state relative permeability has been so far not assessed and is subject to ongoing research.

6. Acknowledgments

The authors would like to acknowledge Holger Ott, Omidreza Amrollahinasab, and Jos Maas for helpful discussions and Tibi Sorop and Yingxue Wang reviewing the manuscript. Luud Heck, Aarthi Thyagarajan, Sherin Mirza and Rene-Edouard Plessix are acknowledged gratefully for support with the GitHub release.

Code availability

Name of the code/library: Core2Relperm

Contact: steffen.berg@shell.com, +31206307087

Hardware requirements: standard workstation computer with Intel Core i7 or i9 or equivalent AMD CPU

(the code was tested on a wide range of Intel CPUs, run times refer to core i9-10885H CPU)

Program language: Python

Software required: Python distribution with `numba` e.g. Anaconda distribution or WinPython

Program size: 5 MByte

The source codes are available for downloading at the link: https://github.com/sede-open/Core2Relperm

References

Abdallah, W., Buckley, J. S., Carnegie, A., Edwards, J., Herold, B., Fordham, E., Graue, A., Habashi, T., Seleznev, N., Signer, C., Hussain, H., Montaron, B., Ziauddin, M., 2007. Fundamentals of Wettability. Oilfield Review 44-61.

Almutairi, A., Othman, F., Ge, J., Le-Hussain, F., 2022. Modified Johnson–Bossler–Naumann method to incorporate capillary pressure boundary conditions in drainage relative permeability estimation. Journal of Petroleum Science and Engineering 210, 110064.

Amrollahinasab, O, Azizmohammadi, S. and Ott, H., 2022. Simultaneous Interpretation of SCAL Data with Different Degrees of Freedom and Uncertainty Analysis, International Symposium of the Society of Core Analysts held in Austin, Texas, USA, 17-22 September 2022, paper SCA2022-33.

Amrollahinasab, O, Azizmohammadi, S. and Ott, H., 2023. Simultaneous interpretation of SCAL data with different degrees of freedom and uncertainty analysis. Computers and Geotechnics 153, 105074.

Anderson, W.G., 1987a. Wettability Literature Survey – Part 4: Effects of Wettability on Capillary Pressure. Journal of Petroleum Technology 39(10), 1283-1300. SPE-15271-PA.

Anderson, W.G., 1987b. Wettability Literature Survey – Part 5: Effects of Wettability on Relative Permeability. Journal of Petroleum Technology 39(11), 1453-1468. SPE-16323-PA.

Al-Menhali, A. S., Krevor, S., 2016. Capillary Trapping of CO_2 in Oil Reservoirs: Observations in a Mixed-Wet Carbonate Rock, Environmental Science & Technology 50, 2727-2734.

Benham, G. P., Bickle, M. J., Neufeld, J. A., 2021A. Two-phase gravity currents in layered porous media. Journal of Fluid Mechanics 922, A7. doi:10.1017/jfm.2021.523

Benham, G. P., Bickle, M. J., Neufeld, J. A., 2021B. Upscaling multiphase viscous-to-capillary transitions in heterogeneous porous media. Journal of Fluid Mechanics 911, A59. doi:10.1017/jfm.2020.1134

Bennion, B., Bachu, S., 2005. Relative permeability characteristics for supercritical CO_2 displacing water in a variety of potential sequestration zones. In: Society of Petroleum Engineers SPE 95547, pp. 1–15.

Bennion, D.B., Bachu, S., 2007. Permeability and relative permeability measurements at reservoir conditions for CO_2–water systems in ultra low permeability confining caprocks. In: Society of Petroleum Engineers SPE 106995, pp. 1–9.

692 Berg, S., Ott, H., 2012. Stability of CO_2-Brine Immiscible Displacement. International Journal of Greenhouse Gas
693 Control 11, 188-203.
694 Berg, S., Oedai, S., Ott, H., 2013. Displacement and Mass Transfer Between Saturated and Unsaturated CO_2-Brine
695 Systems in Sandstone. International Journal of Greenhouse Gas Control 12, 478-492.
696 Berg, S., Unsal, E., Dijk, H., 2020. Non-Uniqueness and Uncertainty Quantification of Relative Permeability
697 Measurements by Inverse Modelling. Computers and Geotechnics 132, 103964.
698 Berg, S., Gao, Y., Georgiadis, A., Brussee, N., van der Linde, H., Dietderich, J., Alpak, F. O., Eriksen, D., Mooijer-
699 van den Heuvel, M., Southwick, J., Appel, M., Wilson, O. B., 2020a, Determination of Critical Gas Saturation by
700 Micro-CT, Petrophysics 61(2), 133-150.
701 Berg, S., Unsal, E., Dijk, H., 2021. Sensitivity and uncertainty analysis for parameterization of multi phase flow
702 models. Transport in Porous Media 140(1), 27-57.
703 Borazjani, S., Hemmatia, N., Behr, A., Genolet, L., Mahani, H., Zeinijahromi, A., Bedrikovetsky, P., Simultaneous
704 determination of gas–water relative permeability and capillary pressure from steady-state corefloods, Journal of
705 Hydrology 598, 126355, 2021
706 Bui, M. et al. 2018. Carbon capture and storage (CCS): the way forward. Energy & Environmental Science 11, 1062-
707 1176.
708 Burnside, N. M. and Naylor, M., 2014. Review and implications of relative permeability of CO_2/brine systems and
709 residual trapping of CO_2. International Journal of Greenhouse Gas Control 23, 1–11.
710 Carden, P. O., Paterson, L., 1979. Physical, Chemical and Energy Aspects of Underground Hydrogen Storage.
711 International Journal of Hydrogen Energy 4(6): 559-569.
712 Cavanagh, A. J., Haszeldine, R. S., 2014. The Sleipner storage site: Capillary flow modelling of a layered CO_2 plume
713 requires fractured shale barriers within the Utsira Formation. International Journal of Greenhouse Gas Control
714 21, 101-112.
715 Corey, A.T.: The interrelation between gas and oil relative permeabilities. 1954. Prod. Monthly. 19(1), 38–41
716 Dake, L.P., 1978. Fundamentals of Reservoir Engineering. Elsevier B.V.
717 Farokhpoor, R., Bjørkvik, B. J. A., Lindeberg, E., Torsæter, O., 2013. Wettability behavior of CO_2 at storage
718 conditions, International Journal of Greenhouse Gas Control 12, 18-15.

719 Flesch, S., Pudlo, D., Albrecht, D., Jacob, A., Enzmann, F. 2018. Hydrogen underground storage Petrographic and
720 petrophysical variations in reservoir sandstones from laboratory experiments under simulated reservoir
721 conditions. International Journal of Hydrogen Energy 43, 20822-20835.
722 Foreman-Mackey, D., Hogg, D. W., Lang, D., Goodman, J., 2012. emcee: The MCMC Hammer, arXiv:1202.3665
723 [astro-ph.IM], DOI:10.1086/670067
724 Gabrielli, P., Poluzzi, A., Kramer, G. J., Spiers, C., Mazotti, M., Gazzani, M., 2020. Seasonal energy storage for zero-
725 emissions multi-energy systems via underground hydrogen storage. Renewable and Sustainable Energy Reviews
726 121, 109629.
727 Gao, Y., Georgiadis, A., Brussee, N., Coorn, A., van der Linde, H., Dietderich, J., Alpak, F. O., Eriksen, D., Mooijer-
728 van den Heuvel, M., Appel, M., Sorop, T., Wilson, O.B., Berg, S., 2021, Capillarity and Phase-Mobility of a
729 Hydrocarbon Gas-Liquid System, Oil & Gas Science and Technology - Revue d'IFP Energies nouvelles 76, 43.
730 Ge, J., Zhang, X., Liu, J., Almutairi, A., Le-Hussain, F., 2022. Influence of capillary pressure boundary conditions
731 and hysteresis on CO2-water relative permeability. Fuel 312, 124132.
732 Hashemi, L., Glerum, W., Farajzadeh, R., Hajibeygi, H., 2021. Contact angle measurement for hydrogen/ brine/
733 sandstone system using captive-bubble method relevant for underground hydrogen storage. Advances in Water
734 Resources 154, 103964.
735 Hashemi, L., Blunt, M., Hajibeygi, H., 2021a. Pore-scale modelling and sensitivity analyses of hydrogen-brine
736 multiphase flow in geological porous media, Scientific Reports 11, 8348. https://doi.org/10.1038/s41598-021-
737 87490-7
738 Hashemi, L., Boon, M., Glerum, W., Farajzadeh, R., Hajibeygi, H., 2022. A comparative study for H_2–CH_4 mixture
739 wettability in sandstone porous rocks relevant to underground hydrogen storage, Advances in Water Resources
740 163, 104165.
741 Hemmati, N., Borazjani, S., Yang, S., Badalyan, A., Genolet, L., Behr, A., Zeinijahromi, A., Bedrikovetsky, P., 2022.
742 Laboratory validation of steady-state-transient test to determine relative permeability and capillary pressure. Fuel
743 321, 123940.
744 Higgs, S., Wang, Y. D., Ennis-King, J., Jackson, S. J., Armstrong, R. T., Mostaghimi, P., 2022. Direct measurement
745 of in-situ hydrogen-water-quartz system relative permeability for underground hydrogen in a depleted gas

reservoir. Proceedings of the Society of Core Analysts 2022 Annual Technical Symposium held in Austin, Texas, USA on 19.-22. September 2022, paper SCA2022-058.

Hogg, D.W., Bovy, J., Lang, D., 2010. Data analysis recipes: Fitting a model to data, arXiv:1008.4686 [astro-ph.IM].

Huang, D.D., Honarpour, M.M., 1998. Capillary end effects in coreflood calculations. J. Petrol. Sci. Eng. 19, 103–117.

Johnson, E.F., Bossler, D.P., Naumann, V.O., 1959. Calculation of relative permeability from displacement experiments. Trans. AIME 216, 370–372.

Iglauer, S., Ali, Muhammad, Keshavarz, A., 2020. Hydrogen wettability of sandstone reservoirs: implications for hydrogen storage. Geophysical Research Letters 48, e2020GL090814.

IPCC, 2005. IPCC Special Report on Carbon Dioxide Capture and Storage, Prepared by Working Group III of the Intergovernmental Panel on Climate Change. Cambridge University Press, Cambridge, United Kingdom/New York, NY, USA.

Krevor, S., Pini, R., Zuo, L. Benson, S. M., 2012. Relative permeability and trapping of CO_2 and water in sandstone rocks at reservoir conditions, Water Resources Research 48, W02532.

Krevor, S., Blunt, M. J., Benson, S. M., Pentland, C. H., Reynolds, C. Al-Menhali, A., Niu, B., 2015. Capillary trapping for geologic carbon dioxide storage – From pore scale physics to field scale implications, International Journal of Greenhouse Gas Control 40, 221-237.

Lake, L.W., 1984. Enhanced Oil Recovery. Prentice Hall.

Lenormand, R., Lorentzen, K., Maas, J.G., Ruth, D., 2016. Comparison of Four Numerical Simulators for SCAL Experiments, International Symposium of the Society of Core Analysts held in Snowmass, Colorado, USA, 21-26 August 2016, paper SCA2016-006.

LeVeque, R.J., 1990. Numerical Methods for Conservation Laws. Lectures in Mathematics, ETH Zürich, Birkhäuser.

Levenberg, K. 1944. A Method for the Solution of Certain Non-Linear Problems in Least Squares. Quarterly of Applied Mathematics, 2(2):164-168.

Lin, Q., Bijeljic, B., Berg, S., Pini, R., Blunt, M. J., Krevor, S., 2019. Minimal surfaces in porous media: pore-scale imaging of multiphase flow in an altered-wettability Bentheimer sandstone, Phys. Rev. E 99, 063105.

Lomeland, F., Ebeltoft, E., Thomas, W.H., 2005. A new versatile relative permeability correlation. International Symposium of the Society of Core Analysts held in Toronto, Canada, 21-25 August, 2005, paper SCA2005-032.

774 Lord, A. S., Kobos, P. H., Borns, D. J., 2014. Geologic storage of hydrogen: Scaling up to meet city transportation
775 demands. International Journal of Hydrogen Energy 39(28): 15570-15582.
776 Lysyy, M., Ersland, G., Fernø, M., 2022. Pore scale dynamics for underground porous media hydrogen storage.
777 Advances in Water Resources, DOI: 10.1016/j.advwatres.2022.104167
778 Lysiyy, M., Føyen, T., Johannesen, E. B., Fernø, M., Ersland, G., 2022a, Hydrogen Relative Permeability Hysteresis
779 in Underground Storage, Geophysical Research Letters 49, e2022GL100354.
780 Maas, J.G., Schulte, A.M., 1997. Computer simulation of Special Core Analysis (SCAL) flow experiments shared on
781 the Internet, International Symposium of the Society of Core Analysts held in Calgary, Alberta, Canada, 1997,
782 paper SCA1997-19.
783 Maas, J.G., Springer, N., Hebing, A., 2019. Defining a sample heterogeneity cut-off value to obtain representative
784 Special Core Analysis (SCAL) measurements, International Symposium of the Society of Core Analysts held in
785 Pau, France, 26-30 August, paper SCA2019-024.
786 Maas, J.G., Flemisch, B., Hebing, A., 2011. Open Source Simulator DUMUX Available for SCAL Data Interpretation,
787 International Symposium of the Society of Core Analysts held in Austin, Texas, USA 18-21 September, 2011,
788 paper SCA2011-08.
789 Maini, B., Coskuner, G., Jha, K., 1990. A comparison between steady-state and unsteady-state relative permeability
790 in viscous oil and water in Ottawa sand. Can. J. Pet. Technol. 29 (2), 72–77.
791 Manasipov, R., Jenei, B., 2020. Automated Interpretation Tool for Synchronous History Matching of Multiple SCAL
792 Experiments with Advance Nurbs representations of Relevant Functions, SPE Europec featured at 82nd EAGE
793 Conference and Exhibition, 8 June, paper SPE-200559-MS.
794 Marquardt, D. 1963. An Algorithm for Least-Squares Estimation of Nonlinear Parameters. SIAM Journal on Applied
795 Mathematics, 11(2):431-441.
796 Masalmeh, S.K, Sorop, T.G., Suijkerbuijk, B.M.J.M., Vermolen, E.C.M., Douma, S., van der Linde, H.A., Pieterse,
797 S.G.J., 2014. Low Salinity Flooding: Experimental Evaluation and Numerical Interpretation, IPTC 17558,
798 presented at the International Petroleum Technology Conference, Doha, Qatar 19-22 January 2014.
799 McClure, J. E., Fan, M., Berg, S., Armstrong, R. T., Berg, C. F., Li, Z., Ramstad, T., 2022. Relative Permeability as
800 a stationary process: energy fluctuations in immiscible displacement, Physics of Fluids 34, 092011.

Moodie, N., Rasmussen, L. Heath, J., Dewers, T., McPherson, B., 2019. Capillary pressure derived relative permeability relationships, AGU 2019 Fall meeting, 09-13 December 2019, San Francisco, CA, USA, DOI: 10.1002/essoar.10501048.1

Newville, M., Stensitzki, T., Allen, D. B., Ingargiola, A., 2014. LMFIT: Non-linear least square minimization and curve-fitting for Python, https://dx.doi.org/10.5281/zenodo.11813

Ott, H., Pentland, C. H., Oedai, S., 2015. CO_2-brine displacement in heterogeneous carbonates, International Journals of Greenhouse Gas Control, 135-144.

Pan, B., Yin, X., Ju, Y., Iglauer, S., 2021. Underground hydrogen storage: Influencing parameters and future outlook. Advances in Colloid and Interface Science 294, 102473.

Pan, B., Liu, K., Ren, B., Zhang, M., Ju, Y., Gu, J., Zhang, X, Clarkson, C. R., Edlmann, K;, Zhu, W. Iglauer, S., 2023. Impacts of relative permeability hysteresis, wettability, and injection/withdrawal schemes on underground hydrogen storge in saline aquifers. Fuel 333, 126516.

Ranaee, E.h, Inzoli, F., Riva, M., Guadagnini, A., 2022. Sensitivity-based Parameter Calibration of Single- and Dual-continuum Coreflooding Simulation Models, Transport in Porous Media 145, 549–587.

Pini, R., Benson, S. M., 2013. Simultaneous determination of capillary pressure and relative permeability curves from core-flooding experiments with various fluid pairs, Water Resources Research 49, 3516-3530.

Ramakrishnan, T. S., Cappiello, A., 1991. A new technique to measure static and dynamic properties of a partially-saturated porous medium. Chemical Engineering Science 46(4), 1157-1163.

Saló-Salgado, L., Haugen, M., Eikehaug, K., Fernø, M, Nordbotten, J. M., Juanes, R. 2023. Direct comparison of numerical simulations and experiments of CO_2 injection and migration in geologic media: value of local data and predictability. arXiv:2301.08875v1.

Saraji, S., Goual, L., Piri, M., Plancher, H., 2013. Wettability of Supercritical Carbon Dioxide/Water/Quartz Systems: Simultaneous Measurements of Contact Angle and Interfacial Tension at Reservoir Conditions, Langmuir 29, 6856-6866.

Rezaei, A., Hassanpouryouzband, A., Molnar, I., Derikvand, Z., Hazeldine, R. S., Edlmann, K., 2022. Relative Permeability of Hydrogen and Aqueous Brines in Sandstones and Carbonates at Reservoir Conditions, Geophysical Research Letters 49, e2022GL099433. https://doi.org/10.1029/2022GL099433

828 Shao, Q., Boon, M., Youssef, A. Kurtev, K., Benson, S. M., Matthai, S. K., Modelling CO_2 plume spreading in highly
829 heterogeneous rocks with anisotropic, rate-dependent saturation functions: A field-data based numeric study of
830 Otway, 2022. International Journal of Greenhouse Gas Control 119, 103699, 2022.
831 Singh, K., Unabaraonye, B. U., Blunt, M. J., Crawshaw, J., 2018. Partial dissolution of carbonate rock grains during
832 reactive CO_2 -saturated brine injection under reservoir conditions, Advances in Water Resources 122, 27-36.
833 Skjaeveland, S.M., Siqveland, L.M., Kjosavik, A., Hammervold, W.L., Virnovsky, G.A., 1998. Capillary pressure
834 correlation for mixed-wet reservoirs. In SPE India Oil and Gas Conference and Exhibition, 17-19 February 1998,
835 New Delhi, India, number SPE 39497.
836 Sorop, T.G., Masalmeh, S.K., Suijkerbuijk, B.M.J.M., van der Linde, H.A., Mahani, H., Brussee, N.J., Marcelis,
837 F.A.H.M., Coorn, A., 2015. Relative permeability measurements to quantify the low salinity flooding effect at
838 field scale. Abu Dhabi International Petroleum Exhibition and Conference held in Abu Dhabi, UAE, 9-12
839 November 2015, number SPE-177865-MS.
840 Szukczewski, M. L., MacMinn, C. W., Herzog, H. J. Juanes, R., 2012. Lifetime of carbon capture and storage as a
841 climate-change mitigation technology, Proceedings of the National Academy of Sciences 109 (14), 5185-5189.
842 Taheriotaghsara, M., 2020a. Enhanced oil recovery methods targeting Danish North Sea chalk reservoirs PhD Thesis,
843 Denmark Technical University.
844 Taheriotaghsara, M., Bonto, M., Eftekhari, A., Nick, H.M., 2020b. Prediction of oil breakthrough time in modified
845 salinity water flooding in carbonate cores. Fuel 274, 117806.
846 Tarkowski, R., Uliasz-Misiak, B., Tarkowski, P., 2021. Storage of hydrogen, natural gas, and carbon dioxide –
847 Geological and legal considerations. International Journal of Hydrogen Energy 46, 20010-20022.
848 Valdez, A.R., Rocha, B.M., Chapiro, G., dos Santos, R.W., 2020. Uncertainty quantification and sensitivity analysis
849 for relative permeability models for two-phase flow in porous media. J. Petrol. Sci. Eng. 192, 107297.
850 Valdez, A. R., Rocha, B. M. da Fonseca Façanha, J. M., de Souza, A. V. O., Pérez-Gramatges, A., Chapiro, A., dos
851 Santos, R. W., 2021. Foam-Assisted Water–Gas Flow Parameters: From Core-Flood Experiment to Uncertainty
852 Quantification and Sensitivity Analysis, Transport in Porous Media, 1-21, https://doi.org/10.1007/s11242-021-
853 01550-0

Yekta, A. E., Manceau, J.-C., Gaboreau, S., Pichavant, M., Audigane, P., 2018. Determination of Hydrogen–Water Relative Permeability and Capillary Pressure in Sandstone: Application to Underground Hydrogen Injection in Sedimentary Formations. Transport in Porous Media 122, 333-356.

Zhou, X., Al-Otaibi, F., Kokal, S., 2019. Relative Permeability Characteristics and Wetting Behavior of Supercritical CO_2 Displacing Water and Remaining Oil for Carbonate Rocks at Reservoir Conditions. Energy & Fuels 33, 5464-5475.

A. Appendix A: Python Code

1.1 Definition of core and fluid data

The rock and fluid properties were defined in a set of variables (which are the ones used for the ground-truth in this work)

```
# core and fluid data
exp_core_length    = 3.9       # cm
exp_core_area      = 12.0      # cm2
exp_permeability   = 100.0     # mDarcy
exp_porosity       = 0.18      # v/v
exp_sw_initial     = SWC       # v/v
exp_viscosity_w    = 1.0       # cP
exp_viscosity_n    = 1.0       # cP
exp_density_w      = 1000.0    # kg/m3
exp_density_n      = 1000.0    # kg/m3
```

which are then used in the displacement model

```
#Define 1D2P displacement model

model1 = DisplacementModel1D2P(
    NX=50,
    core_length    = exp_core_length,
    core_area      = exp_core_area,
    permeability   = exp_permeability,
    porosity       = exp_porosity,
    sw_initial     = exp_sw_initial,
    viscosity_w    = exp_viscosity_w,
    viscosity_n    = exp_viscosity_n,
    density_w      = exp_density_w,
    density_n      = exp_density_n,
    rlp_model      = rlp_model1,
    cpr_model      = cpr_model1,
    time_end       = T_END,
    rate_schedule  = Schedule,
    movie_schedule = Movie_times, # Same timesteps as experimental data
 )
```

1.2 Numerical Solver model and NUMBA just-in-time compiler

The numerical solver was a 1D explicit finite difference scheme with time stepping control. It handled two-phase incompressible flow with capillarity and gravity in unidirectional flow, i.e. no counter-current imbibition.

The solver was contained in the `displacementmodel1D2P001.py` library (called from the `numba` just-in-time-compiler).

```
@numba.njit
def solve_1D2P_version1(
           N=21,
           cpr_model=None,
           rlp_model=None,
           cpr_multiplier=1.0,
           viscosity_w=1.0,
           viscosity_n=1.0,
           gvhw = 0.0,
           gvhn = 0.0,
           sw_initial=0,
           tD_end=0.2,
           follow_stops = False,
           t_stops = [], # user imposed stops
           s_stops = [], # scale factors
           f_stops = [], # fractional flows
           max_nr_iter=10,
           nr_tolerance=1e-3,
           verbose=1,
           max_dsw = 0.1,
           max_num_step=1e20,
           max_step_size = 0.01,
           start_step_size = 0.001,
           refine_grid = False,
           reporting = True,
          ):
```

which was then called through an object class.

```
class DisplacementModel1D2P(object):

    def __init__(self,
                 core_length=None,
                 core_area=None,
                 permeability=None,
                 porosity=None,
                 sw_initial=None,
                 viscosity_w=None,
                 viscosity_n=None,
                 density_w=None,
                 density_n=None,
                 gravity_multiplier=1.0,
                 cpr_multiplier=1.0,
                 time_end=None,
                 rlp_model=None,
                 cpr_model=None,
                 rate_schedule=None,
                 movie_schedule=None,
                 NX=50,
                 verbose=False,
                 max_step_size=1.0,
                 start_step_size=0.001,
```

```
                    refine_grid=True,
                    max_nr_iter=25,
                    nr_tolerance=1e-10,
                   ):
```

1.3 Schedule of flow rates and injection conditions

The flow solver then runs over a pre-defined schedule where flow rates and fractional flows were defined

```
#times in min, injrate in cm3/min

Schedule = pd.DataFrame(
     [[0.0,    0.1, 1.0],
      [1.4,  2*0.1, 1.0],     # bump floods
      [1.6,  5*0.1, 1.0],
      [1.8,  10*0.1, 1.0]],    # bump floods
    columns=['StartTime','InjRate','FracFlow'] )
```

1.4 Objective Function

```
uss_matchobj = USSMatchObjective1(
    model=model1,
    dp_weight=1, op_weight=1, sw_weight=1,
    dp_data=expdataHIS,
    dp_error=0.01,
    op_data =expdataHIS,
    op_error = 0.05,
    sw_profile_times=expdataHISsattimes,
    sw_profile_data =expdataHISsatprofiles,
    sw_error = 0.01,
    dp_switch_time=0, # switch from delta_P_o to delta_P_w at this time
)
```

1.5 Minimizer with Least Squares or Markov Chain Monte Carlo

A) Code example for gradient-based least-squares minimization with Levenberg-Marquardt

```
result_pckr = Minimizer(uss_matchobj, params_pckr
                ).least_squares(diff_step=1e-4,verbose=2)
```

B) Code example for Markov-chain Monte Carlo using `emcee` through the `minimizer` interface in `lmfit`

```
result_pckr = Minimizer(uss_matchobj, params_pckr, nan_policy='omit'
                ).emcee(steps=20000, burn=300, thin=20, is_weighted=True)
```

List of Figures

13. Figure 13 Cross-correlation between model parameters employed in the fit from Figure 11 and Figure 12. Many cases of strong correlation (or anti-correlation) suggest that the problem is either over-parameterized or under-constrained.
14. Figure 14 Error ellipses for the case from Figure 11 and Figure 12 but computed by MCMC (20000 iterations).
15. Figure 15 Match of the flow model to the synthetic data set from Figure 9. In the match both relative permeability and capillary pressure very varied, including residual oil saturation. 11 saturation profiles (C) were included in the objective function (shown in red). A very good match was observed for pressure drop (A), production curve (B) and also for the saturation profiles (C) but overall similar quality as in the match in in Figure 11 where no saturation profiles were considered in the objective function.
16. Figure 16 Relative permeability uncertainty ranges for the match from Figure 15 where 11 saturation profiles had been considered in the objective function. The uncertainty ranges notably decreased compared to the case without saturation profiles in the objective function, shown in Figure 12C.
17. Figure 17 Cross-correlation between model parameters employed in the fit from Figure 15 and Figure 16. Compared with the case without saturation profiles in the objective function (Figure 13), the cross correlations significantly decreased, but are still considerably large for several parameter pairs.
18. Figure 18 Error ellipses for the case from Figure 15 and Figure 16 but computed by MCMC (20000 iterations). Similar as the reduction of uncertainty ranges for relative permeability (Figure 12C vs. Figure 16) and reduction of cross correlations from the least squares fit (Figure 13 vs. Figure 17) by incorporating 11 saturation profiles the error ellipses significantly shrink compared with the case where no saturation profiles were considered in the objective function (Figure 14).
19. Figure 19 Match of the flow model to the synthetic data set from Figure 9 adding 3 additional flow rate steps where the flow rate is increased by 2x, 5x and 10x. In the match both relative permeability and capillary pressure very varied, including residual oil saturation. 19 saturation profiles (C) were included in the objective function (shown in red). A very good match was observed for all parameters.
20. Figure 20 Relative permeability and capillary pressure function of the match for the match from Figure 19 where 3 bump floods and 19 saturation profiles had been considered in the objective function. The match is now very close to the ground truth. By including the bump floods, relative permeability uncertainty ranges have significantly decreased compared with the two cases without bump floods (Figure 12C and Figure 16) and are now overall in the range of the added noise.
21. Figure 21 Cross-correlation between model parameters employed in the fit from Figure 19 and Figure 20. Overall, the cross correlations further decreased compared with the cases without bump flood (Figure 13 and Figure 17). But there are cases where cross correlations increased.
22. Figure 22 Relative permeability and capillary pressure function considering 3 bump floods and 19 saturation profiles in the objective function but matching only the effective pressure drop and not water and oil pressure drop independently (because these are in most experiments not independently accessible). The results are very similar to the case where both water and oil pressure drop are used (Figure 20) i.e. identical within the uncertainty.
23. Figure 23 Cross-correlation between model parameters employed in the fit from Figure 22 where only one effective pressure drop has been considered which reflects the experimental reality in most cases. Compared with the situation where both water and oil pressure drops were considered as independent parameters in the objective function (Figure 21), the correlations are very comparable.
24. Figure 24 Modified ground truth where the relative permeability (A) is kept the same as in the previous cases but the capillary pressure (B) is increased by a factor 10 compared with the ground truth from Figure 9. Also the length of the core is reduced by half. As a consequence, the capillary dispersion zone (Figure 10) is poorly resolved over the length of the sample. As a consequence, the uncertainty range for relative permeability significantly increases compared with Figure 22C.
25. Figure 25 Relative permeability uncertainty ranges varying both relative permeability and capillary pressure-saturation functions for production curve and pressure drop only (A, see also Figure 12C), considering 5 saturation profiles (B, see also Figure 16) and 11 saturation profiles (C, see also Figure 16) and including 3 bump floods at 2x, 5x and 10x of the injection velocity (D, see also Figure 20). By including more experimental data to constrain the solution the uncertainty range systematically decreases, until it converges against the ground truth (Figure 9A) within the uncertainty range of the added noise.